

Commissioning the Linac Coherent Light Source injector

R. Akre, D. Dowell, P. Emma, J. Frisch, S. Gilevich, G. Hays, Ph. Hering, R. Iverson, C. Limborg-Deprey, H. Loos, A. Miahnahri, J. Schmerge, J. Turner, J. Welch, W. White, and J. Wu

SLAC, Stanford, California 94309, USA

(Received 17 November 2007; published 12 March 2008)

The Linac Coherent Light Source is a SASE x-ray free-electron laser (FEL) project presently under construction at SLAC [J. Arthur *et al.*, SLAC-R-593, 2002.]. The injector section, from drive laser and rf photocathode gun through first bunch compressor chicane, was installed in the fall of 2006. The initial system commissioning with an electron beam was completed in August of 2007, with the goal of a 1.2-micron emittance in a 1-nC bunch demonstrated. The second phase of commissioning, including second bunch compressor and full linac, is planned for 2008, with FEL commissioning in 2009. We report experimental results and experience gained in the first phase of commissioning, including the photocathode drive laser, rf gun, photocathode, S-band and X-band rf systems, first bunch compressor, and the various beam diagnostics.

DOI: [10.1103/PhysRevSTAB.11.030703](https://doi.org/10.1103/PhysRevSTAB.11.030703)

PACS numbers: 41.60.Cr

I. INTRODUCTION

The months of April through August 2007 were spent commissioning the Linac Coherent Light Source (LCLS) injector. This is the first phase of machine commissioning, with the second phase starting in December of 2007 after a 3-month downtime, and the final phase in November of 2008, culminating in free-electron laser (FEL) light in 2009. First electrons from the new photocathode rf gun were observed on April 5 and beam was quickly established to the nominal injector energy of 250 MeV in the main SLAC linac on April 14, 2007. Over the next five months all injector systems were commissioned and the beam accelerated to as high as 16 GeV at the end of the SLAC linac. The bunch charge of 1 nC and measured transverse normalized emittance of 1.2 microns (at 135 MeV) meet the design brightness requirements of the LCLS. A list of typical measured machine parameters is shown in Table I, including “design” values at 1 nC of bunch charge.

II. DESCRIPTION OF THE INJECTOR

Figure 1 shows the major components of the LCLS injector located at the 2 km point of the 3-kilometer SLAC linac. The below-ground, off-axis housing was built during the original construction of the linac in 1962 [1], anticipating future injectors such as the LCLS.

The LCLS injector begins with a photocathode rf gun followed by two modified SLAC S-band (2.856 GHz) linac sections (L0a and L0b) producing a single electron bunch at a 10 to 30-Hz repetition rate (120 Hz in 2009) with an energy of 135 MeV and up to 1 nC of bunch charge. A low-energy (6 MeV) spectrometer is included just after the rf gun and the cathode drive laser is located above ground in a reconstructed alcove above the injector vault.

The 135-MeV beam is deflected onto the main linac axis by a two-dipole 35-degree achromatic bend. With these

magnets switched off, the beam can optionally be transported to a 35-degree spectrometer for refined energy spread measurements. This spectrometer also allows the LCLS injector to operate simultaneously when a high-energy (30 GeV) beam is being accelerated in the 3-km linac. Once on the axis of the main linac, the LCLS electrons are accelerated to 250 MeV in three 3-m long S-band accelerating structures (L1S) before entering the first bunch compressor chicane (BC1). Located between these structures and BC1 is a 60-cm long X-band (11.424 GHz) 4th harmonic rf accelerating structure, which straightens the beam’s longitudinal phase space for more linear bunch compression. Beam diagnostics for charge, position, energy, energy spread, beam phase,

TABLE I. Design and typical measured parameters.

Parameter	Symbol	Design	Measure	Unit
Final injector e^- energy	$\gamma_0 mc^2$	135	135	MeV
BC1 e^- energy	$\gamma_1 mc^2$	250	250	MeV
End of linac e^- energy	$\gamma_L mc^2$	14	16	GeV
Bunch charge	Q	1	1	nC
Initial bunch length (FWHM)	Δt_0	9	11	ps
Final bunch length (FWHM)	Δt_f	2.3	0.4–11	ps
Initial peak current	I_{pk0}	100	95	A
Projected normal emittance ^a	$\gamma \epsilon_{x,y}$	1.2	1.2	μm
Slice normal emittance ^a	$\gamma \epsilon_{x,y}^s$	1.0	0.9	μm
Slice energy spread (rms)	σ_E	<5	<6	keV
Single bunch repetition rate	f	120	10–30	Hz
rf gun field at cathode	E_g	120	115	MV/m
Laser energy on cathode	u_1	250	300	μJ
Laser wavelength	λ_1	255	253	nm
Laser spot diameter on cathode	$2R$	2.0	1.3	mm
Cathode quantum efficiency	QE	6	3.7	10^{-5}
Commissioning duration	...	8	5	month

^aTransverse emittance values are representative of 95% of the core bunch charge, as described below.

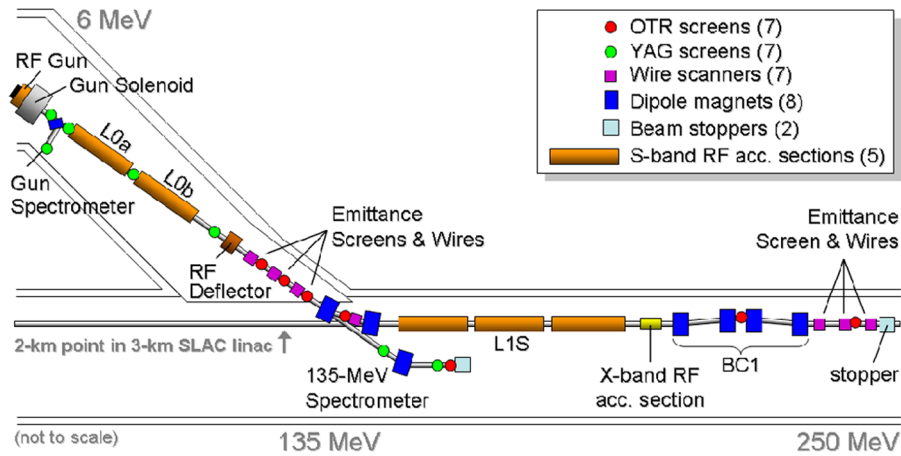


FIG. 1. (Color) The LCLS injector, from gun through first bunch compressor (BC1), with gun located in a separate, off-axis enclosure at the 2/3-point along the SLAC linac.

phase-space matching, bunch length, and emittance are located both upstream and downstream of the BC1, including time-resolved bunch measurements using an S-band transverse rf deflector. An insertable beam stopper is included six meters downstream of BC1 to allow aggressive injector tune-up without sending beam down the main linac.

A “laser-heater” system used to Landau-damp the microbunching instability [2] by increasing the uncorrelated energy spread in the beam will not be installed until the fall of 2008.

III. DRIVE LASER

The gun’s copper cathode is illuminated by a UV laser operating at 253 nm delivering up to 500 microjoules per pulse at 30–120 Hz. In addition to the wavelength and energy, the laser must meet stringent stability and reliability requirements as well as strict transverse and longitudinal shaping specifications.

The drive laser was manufactured by *Thales Laser* and is a frequency tripled, chirped-pulse amplification system based on Ti:sapphire [3]. The system consists of a mode-locked Ti:sapphire oscillator, followed by a pulse stretcher, a Dazzler for pulse shape control, a regenerative amplifier, two multipass amplifiers, a compressor, and finally a frequency tripler, as shown in Fig. 2. The amplifiers are pumped at 120 Hz (mostly 30 Hz in commissioning) by two frequency doubled, Q-switched, qcw-diode-pumped Nd:YAG lasers (*Thales Jedi*). The amplifier produces 25 mJ per pulse at 760 nm with adjustable pulse duration between 3 and 20 ps. After tripling, the energy per pulse is typically 1.5–2.5 mJ at 253 nm. The system was designed to produce a flattop temporal profile, which was not fully achieved during initial commissioning. One of the optimal temporal profiles measured during commissioning with the scanning cross correlator (see below) is shown in Fig. 3.

Work with the vendor after the first commissioning run, however, has greatly improved the temporal shape (not shown here).

Drive laser commissioning involved verification of the specifications and characterization of the optical transport system, diagnostics, and controls. The first part of the transport system is the spatial shaping. Initially an aspheric telescope was used to change the spatial profile from Gaussian to flattop. During commissioning this system produced a high-energy loss and was very sensitive to alignment. As a result, the design was changed to a simple imaged, overfilled aperture (laser iris). This provided a similar shape with higher energy and much less sensitivity to alignment.

The most critical part of transport system commissioning was installation and verification of the virtual cathode. The virtual cathode camera sits in an equivalent plane and provides a monitor of the position and shape of the drive

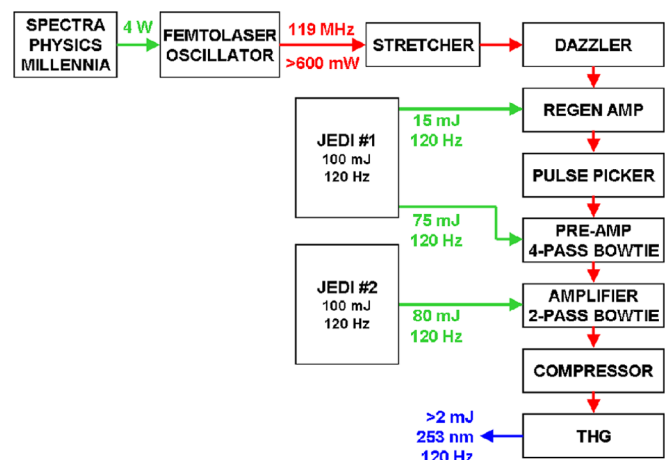


FIG. 2. (Color) Block diagram of the gun drive laser designed and built by *Thales Lasers*.

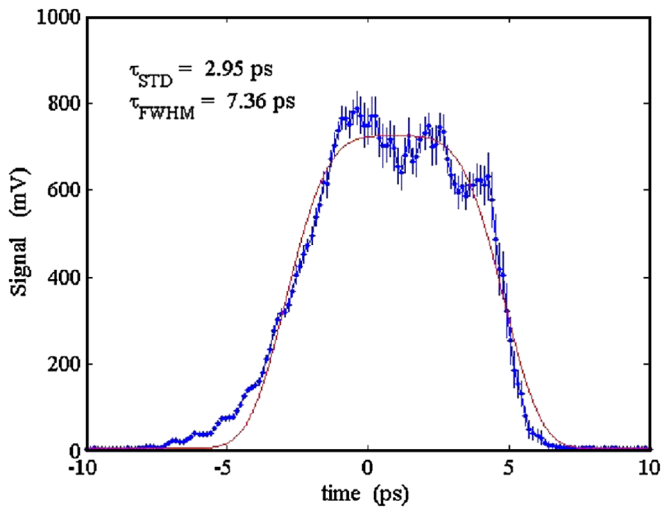


FIG. 3. (Color) Laser temporal profile, with 7.4-ps FWHM pulse length, measured (blue) on the scanning cross correlator, fit with an n th-order super-Gaussian curve (red): $f(t) = A \cdot \exp\{-|(t - t_0)/(2^{1/2}\sigma)|^6\}$.

laser spot on the cathode. A typical image of the virtual cathode taken during commissioning is shown in Fig. 4. Again, work with the vendor later, in the fall of 2007, has greatly improved the spatial shape (not shown here).

The UV light illuminates the cathode using near normal incidence with a symmetric pair of in-vacuum metal mirrors 50 cm downstream of the cathode and just 6.9 mm

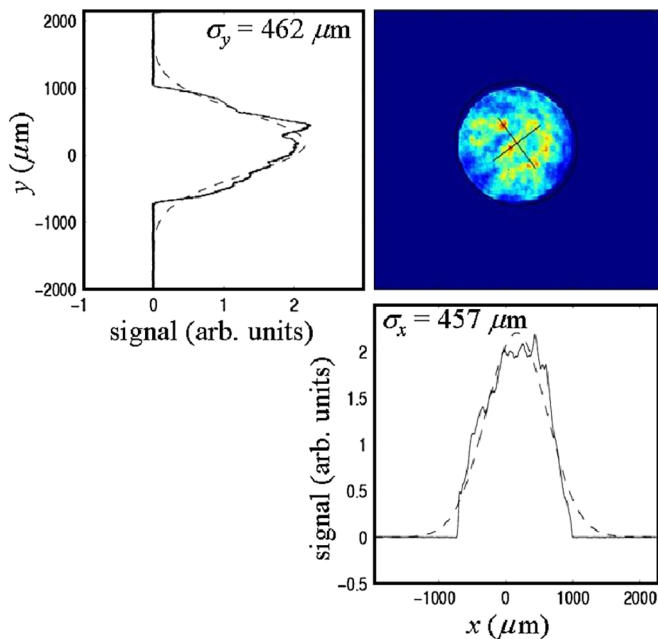


FIG. 4. (Color) The drive laser spot on the virtual cathode with horizontal (x) and vertical (y) projections over the full image. Gaussian (dashed) curves with the same rms are simply overlaid for comparison.

horizontally off axis. Only one mirror is actually used but the symmetric pair avoids transverse wakefields.

The laser is run at a constant energy and rate with a constant thermal load. Control of repetition rate is accomplished by using a pulse slicer to gate the system, allowing pulses to reach the cathode on demand, including 10-Hz, 1-Hz, or single-shot rate control. Amplitude control is accomplished by rotating a wave plate within the tripler. This changes the pulse energy while maintaining a constant thermal load on the amplifier system. Other controls involve pointing and centering feedback loops at several points throughout the transport system, allowing the control system to “lock” the position on the cathode to a specified location. Finally, calibrated energy meters record the pulse energy at various points throughout the transport system, most importantly at a point representing the cathode.

Temporal characterization is accomplished by use of two independent diagnostics. A *Hamamatsu Fesca 200* with 1-ps temporal resolution in the UV is used to directly measure the temporal profile. Both scanning and single-shot cross correlators were built, which allow the temporal profile to be measured by mixing the UV pulse with a <30 -fs IR pulse from the seed oscillator in a beta barium borate crystal (see Fig. 3). The cross correlators have proven to be very robust and reliable and are fully integrated into the controls system.

Drive laser parameters are listed in Table II. With stable UV energy on the cathode, the relative electron charge stability was measured at 1.1% rms at 1 nC over 1 min at a 10-Hz electron repetition rate. This was measured using the sum signal from a stripline beam position monitor (BPM) just after the gun, recording each of 600 sequential beam pulses. The long-term variation is controlled using a feedback loop which varies the laser energy with an adjustable wave plate inside the IR-to-UV frequency tripler. Similarly, the centroid position variation of the laser spot was recorded late in the run, after many improvements, at 11 μm rms in both x and y at 10 Hz over about 1 min. With respect to a round laser rms spot size of $\sigma_R \approx 0.45$ mm (0.7 mm hard-edged radius), the relative rms position jitter

TABLE II. Typical drive laser parameters.

Parameter	Symbol	Value	Unit
UV wavelength on cathode	λ_1	253	nm
Spot diameter on cathode (edge)	$2R$	1.3	mm
Relative energy stability (rms)	σ_E/E	1.2	%
Pulse duration (FWHM)	Δt_{fw}	6	ps
Timing jitter with respect to rf (rms)	σ_t	0.16	ps
x and y centroid jitter (rms)	$\langle x, y \rangle / \sigma_R$	2.5	%
UV energy before transport	E_{UVb}	1.5	mJ
UV energy on cathode	E_{UVc}	0.3	mJ
Repetition rate	f	30–120	Hz
Unscheduled downtime/(6 months)	$\Delta\tau/\tau_0$	2	%

is just 2.5% with laser positioning feedback stabilization switched on. The stability levels with feedback loops switched off were not studied.

The laser oscillator synchronization is performed by controlling a piezoelectric element which adjusts the length of the mode-locked oscillator. This control is set by a feedback circuit which measures the laser phase relative to a 476-MHz reference signal from the low-level rf system. The box functions as a phase detector and feedback amplifier, however its internal design is proprietary to *Femtolaser*. The typical measured short-term (< 1 min) laser phase jitter is < 0.2 ps rms (i.e., < 0.2 degrees of S-band) with respect to the rf reference phase. Slow phase control of the laser is maintained by measuring the phase of the 119-MHz mode-locked signal from the low-level rf system. This phase is maintained by adjusting the phase of the 476-MHz reference sent to the laser through a software feedback loop.

IV. THE PHOTOCATHODE rf GUN

The LCLS photocathode rf gun has been described elsewhere [4–6] and only its general features are summarized here (see Fig. 5). The gun fields are fully rotationally symmetric by incorporating dual feed (to eliminate dipole fields) and a racetrack geometry (to cancel quadrupole fields induced by the dual feed) for the full cell into which the rf is coupled.

Since this gun is the sole electron source for the LCLS user facility, it needs to operate reliably at the relatively high repetition rate of 120 Hz as well as producing exceptional beam quality. This was done by making several changes to the BNL/SLAC/UCLA gun design.

The gun was made more reliable by replacing the commonly used azimuth angle rf coupling with much larger z -coupled ports running the full length of the cell. This approach combined with careful design of the lip radii

greatly reduced the pulsed heating, which otherwise would have limited gun lifetime. In addition, any field emission from tuning slugs was eliminated by using deformation tuners, which were not needed during the tuning process. Finally, the shape of the iris between the two cells was modified to reduce its surface fields below that of the copper cathode (see Fig. 6).

The resulting cathode surface field is approximately 10% higher than the iris fields. With these modifications, the gun was easily conditioned to 120 MV/m and 60 Hz repetition rate. Conditioning at 120 Hz was limited to 107 MV/m due to excessive heating of the gun probes, a limitation which will be corrected by the installation of redesigned probes in early 2008. Therefore, to reduce any risk of damaging the gun due to overheating of the probes, it was decided to limit the repetition rate to 30 Hz and 115 MV/m during the 2007 commissioning run. As a result, the gun operated nearly continuously at 30 Hz for more than 3×10^8 pulses from April 5 to August 24, 2007.

Another important innovation of the gun which improved its beam quality was to greatly increase the frequency separation of the 0-mode and π -mode. Previous S-band guns had been built with 3.2-MHz separation, resulting in excitation of the undesired 0-mode by the low frequency components of rf envelope waveform, allowing it to beat against the π -mode. The presence of the 0-mode increases the correlated energy spread and unbalances the fields between the two cells during both transient and steady state conditions [4,5]. Increasing the mode separation to 15 MHz greatly reduces excitation of the 0-mode, giving a pure π -mode in the gun.

Also included in the injector design is a short, low-energy spectrometer immediately after the gun at about 6 MeV (see Fig. 7). The gun rf phase and amplitude are

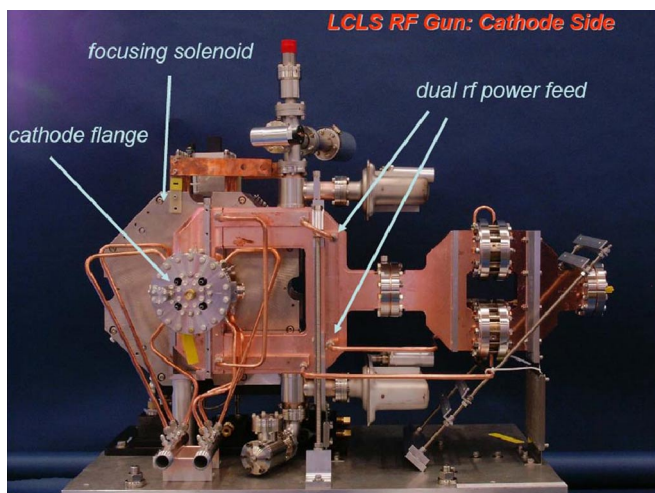


FIG. 5. (Color) The LCLS gun viewed from the cathode side with dual rf feed, cathode flange, and focusing solenoid.

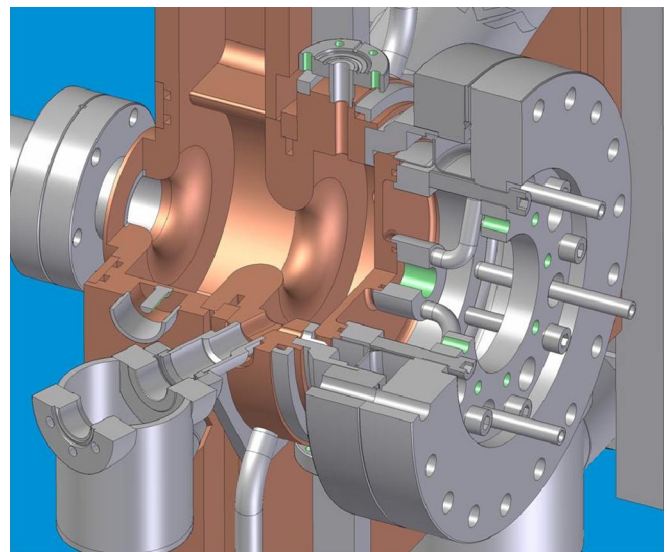


FIG. 6. (Color) The LCLS gun in cut-away view showing the full and half cells with the cathode flange at right.

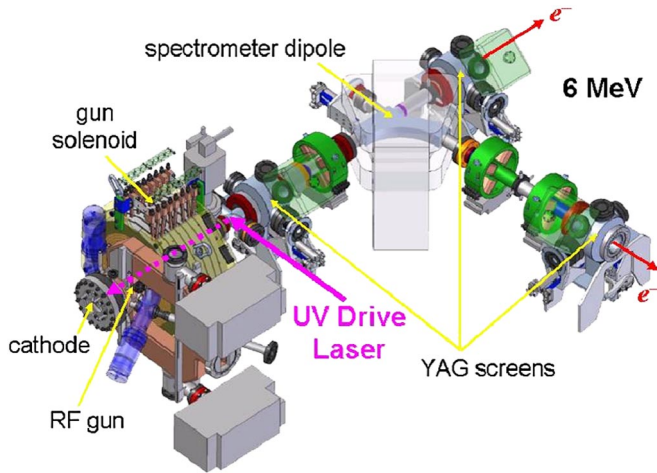


FIG. 7. (Color) The gun and gun-to-linac (GTL) transport, including spectrometer, YAG screens, and solenoid. The drive laser actually enters on the opposite side. The first (green) quadrupole magnet after the gun was never installed since it was determined to be unnecessary and also demonstrated somewhat unpredictable remnant fields.

calibrated using the YAG screen and BPM in this spectrometer line. The gun-to-linac (GTL) line, with spectrometer dipole switched off, includes two BPMs, steering coils, a charge toroid and Faraday cup immediately after the gun, and two YAG screens at 0.6 m and 1.4 m from the cathode. The toroid and Faraday cup were not functional during the commissioning due to installation errors, causing some initial uncertainty in the bunch charge which was resolved by taking beam through the SLAC linac with its well established charge monitors.

The entire GTL beamline from the gun exit to the entrance of the first linac section has been designed to mitigate wakefields. This includes tapering of the beam tube through the gun solenoid, the vacuum valve after the gun solenoid, all bellows, the YAG crosses, and the vacuum chamber for the gun-spectrometer magnet. The beamline is pumped through longitudinal slots to minimize the wakes.

The gun is vacuum pumped through the two large z -coupling ports on the full gun cell (described above) using a 40-liter/sec ion pump on each waveguide feed. These pumps are shown in Fig. 7 as gray boxes to the side, and above and below the rf input flange. A cold cathode gauge mounted on the upper rf waveguide is used to measure the gun vacuum pressure. The quiescent pressure (with rf power off and gun valve closed) is 2×10^{-10} Torr. With the gun valve open, the vacuum rises to 1×10^{-9} Torr, and with rf power applied at 30 Hz the pressure is 1.5×10^{-9} Torr. The initial high-power rf processing of the gun was performed in the SLAC Klystron Lab as described in Ref. [6].

In operation, the relative phasing between the gun and laser is established by running a ‘‘Schottky scan,’’ which varies the laser phase while measuring the accelerated

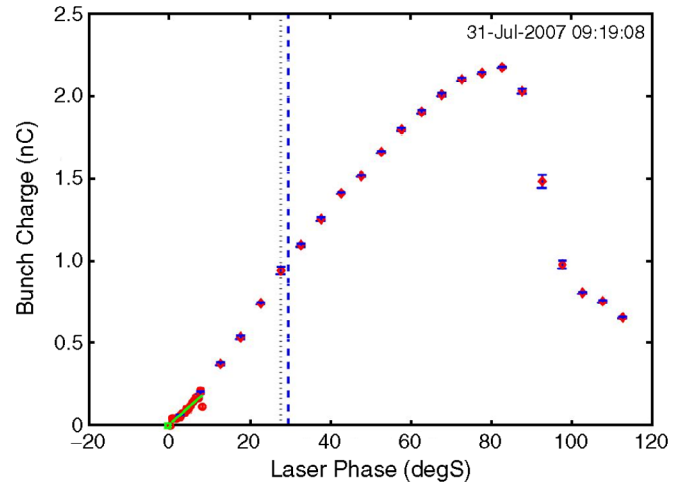


FIG. 8. (Color) An example Schottky scan where the laser phase is varied and the bunch charge measured. The phase is set 30 degS from the zero-crossing point (at 0). The initial phase (before the scan) is shown as a dotted vertical line and the new phase (after the scan) is shown as a dashed blue vertical line.

bunch charge after the gun. An example Schottky scan is shown in Fig. 8, where after the scan the laser phase is finally set 30 degS (i.e., degrees of S-band phase at $f = 2856$ MHz) off the zero-crossing phase. This produces 1 nC in the figure and approximately optimizes the beam brightness. At this launch phase the bunch exits the gun with approximately minimum energy spread and minimal rf emittance growth [7,8].

The beam energy and energy spread immediately after the gun is measured using the gun spectrometer (see Fig. 7). The data is taken using a digital camera viewing a 100- μ m thick YAG crystal after the spectrometer bend. The minimum rms value of 21 keV occurs near 20 degS

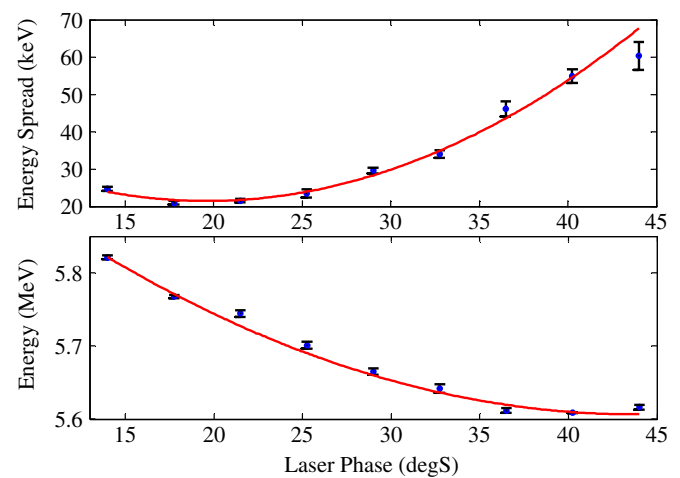


FIG. 9. (Color) The rms energy spread (top) and energy (bottom) as a function of laser phase. Here the cathode peak field was 110 MV/m and laser pulse length 6 ps FWHM. Red curves are a parabolic fit to the data.

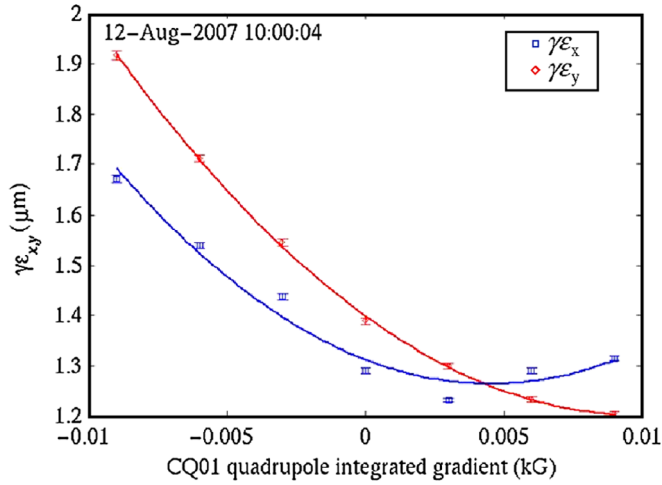


FIG. 10. (Color) Horizontal (blue) and vertical (red) emittance at 135 MeV and 1 nC optimized (parabolic fit) by varying the gun-solenoid’s normal quadrupole coil field, *CQ01*.

launch phase, as shown in Fig. 9, and is due to time-correlated energy spread. The uncorrelated energy spread is determined to be less than 6 keV (at 150 pC), similar to that measured in the GTF [9,10] and FLASH at DESY [11], although at a lower charge.

The measured transverse emittance is minimized with several optimization scans, including the main solenoid strength (see Fig. 31), the beam trajectory, and also two small quadrupole coils incorporated into the gun-solenoid magnet. These coils were included to cancel a small quadrupole field error measured at the ends of the gun solenoid. One of these coils is wound to produce a “normal” quadrupole and a second is wound as a “skew” quadrupole. The coils are single wires which run the length of the gun

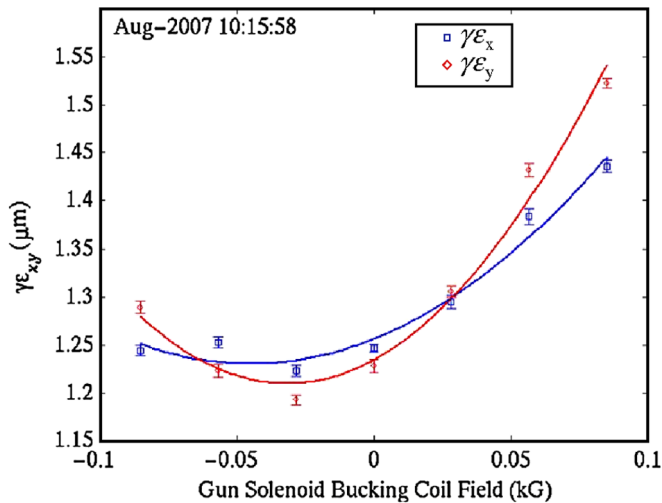


FIG. 11. (Color) Horizontal (blue) and vertical (red) emittance at 135 MeV optimized (parabolic fits) by varying the gun-solenoid’s bucking coil field. The minimum emittance occurs close to the expected value of -0.027 kG.

solenoid (~ 20 cm). The coil excitation currents are empirically tuned while measuring the x and y emittance at 135 MeV, as shown in Fig. 10. Significant improvements in the emittance (10%–30%) are observed with these weak quadrupole coils excited. The final settings are two to three times stronger than is required to cancel the measured solenoid quadrupole field errors. The need for these stronger fields to reduce the emittance is not yet understood.

In addition to these quadrupole coils, a gun-solenoid bucking coil is included to cancel a small, measured (27 Gauss nominal) longitudinal field on the cathode. The very precise emittance measurements allow the bucking coil setting to be confirmed empirically as shown in Fig. 11. The emittance measurement resolution in these optimization scans is about $0.02 \mu\text{m}$ (i.e., 2%, based upon statistical errors only), allowing a clear, reproducible minimum.

V. THE CATHODE

The quantum efficiency (QE) from the copper cathode was quite low for the first two months of commissioning. To complicate the issue, the QE had the appearance of being even lower due to incorrect charge measurements. Once the beam was transported through the main linac, its charge was more accurately measured using well-known SLAC charge monitors. This correction was a factor of 1.45, while the QE was initially 15 times lower than the design requirement.

In order to understand the poor cathode performance, the cathode was imaged using two different methods: (1) with white light and a camera in a near normal-incidence reflection geometry, and (2) using the gun solenoid to create a point-to-point image of the cathode photoemission on the second YAG screen [12]. Illumination for the white light image was done by directing light through the UV optics and vacuum window, and reflecting light off the in-vacuum mirror onto the cathode. A digital camera viewed the cathode through the vacuum window using the opposing in-vacuum mirror (installed for wakefield compensation). The photoemission imaging was done at approximately 10 pC of bunch charge in order to minimize space charge forces blurring the image. A comparison of these two methods of imaging is shown in Fig. 12 for measurements performed toward the beginning of the commissioning period. The resolution in both is excellent and the correspondence between the white light features and the areas of high photoemission is striking.

The initial QE at the start of commissioning was approximately 0.4×10^{-5} , which is 15 times lower than the design specification of 6.0×10^{-5} . This very low QE limited the maximum beam charge to 300 pC during the first half of commissioning. However, reducing the laser size on the cathode during emittance studies also increased the laser fluence to the degree that vacuum activity in the

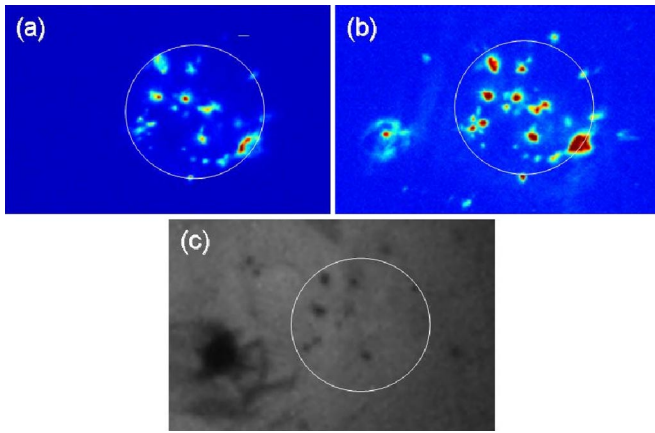


FIG. 12. (Color) Electron emission images on a YAG screen 1.4 m from the cathode, (a) and (b), taken on June 23, and images of the cathode taken using a white light source and camera, (c), taken on June 20. Image (a) is taken with the laser iris set for a 1.3-mm spot diameter and image (b) is taken with the iris fully open. The circle outlines the nominal 1.3-mm diameter laser illumination area.

form of low-level rf arcs were observed, which began to clean the cathode. The result was a fortuitous, steady rise in QE during the last three months of commissioning as can be seen in Fig. 13 (June 4 through August 23).

The cathode QE before and after mild laser cleaning is shown in Fig. 14. The cleaning was done with the gun rf set at two power levels: 5.75 MeV final electron energy (110 MV/m peak cathode field) and 1 MeV (19 MV/m peak field). The gun pressure vacuum and laser energy are shown in Fig. 15 during cleaning at these two gun fields.

The laser-rf phase was nominal at 30 degS from the zero crossing. The laser fluence was approximately 360 μJ per

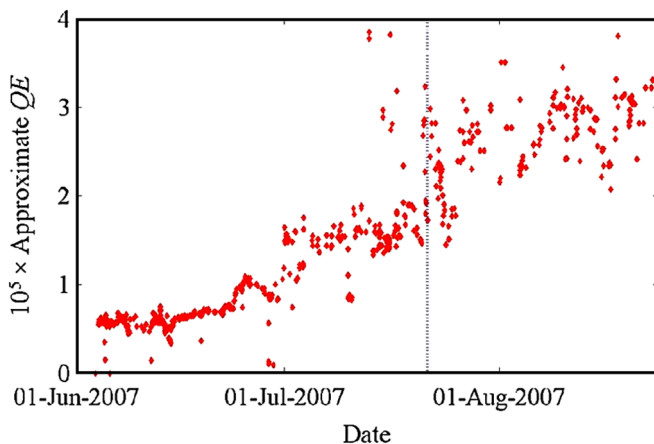


FIG. 13. (Color) The approximate quantum efficiency (QE) during the past three months of commissioning. The vertical line indicates July 21 when the cathode was lightly cleaned with the drive laser at a higher fluence. The large scatter here is due to the crude (temporary) method used for this routine estimate, which is executed with each Schottky scan.

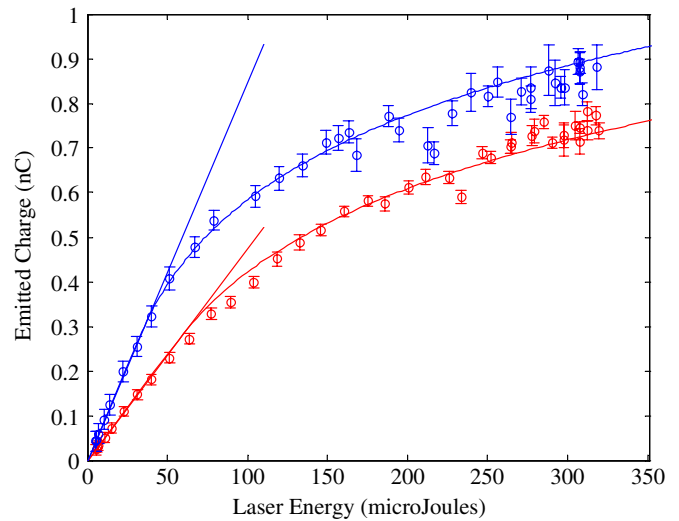


FIG. 14. (Color) The measured charge vs laser energy before (red) and after (blue) laser cleaning. The slopes of the straight lines give the QE and indicate the linearly increasing emitted charge with laser energy in the absence of space charge limited emission. The initial QE was 2.3×10^{-5} and after mild laser cleaning it was 4.1×10^{-5} .

square millimeter in a 0.67-mm diameter cathode laser spot which was slowly moved over a 2-mm by 2-mm area. The dwell time was 10 seconds at each position with a 100- μm step size. The initial and final QE values were 2.3×10^{-5} and 4.1×10^{-5} , respectively, measured at the nominal peak cathode field of 110 MV/m and launch phase of 30 degS from the zero crossing, giving a cathode field of 55 MV/m during photoemission. The QE is determined by measuring the bunch charge as a function of the drive laser energy. Figure 14 shows the measured QE before and after laser cleaning. The QE is given by the slope evaluated

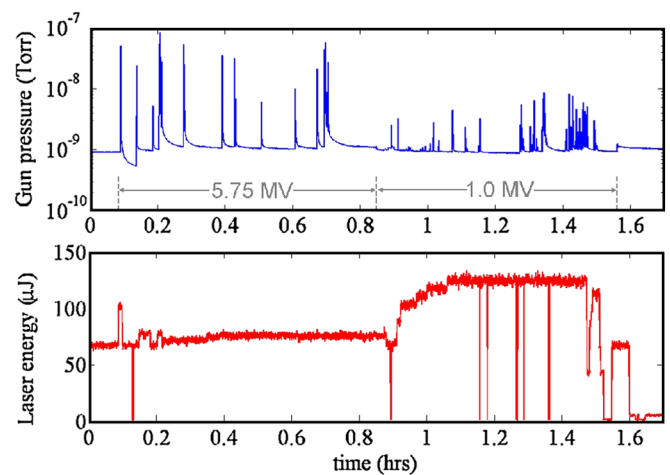


FIG. 15. (Color) The gun vacuum pressure (top-blue) and the laser energy on the cathode (bottom-red) during cleaning of the cathode at 5.75 MV, and later at 1.0 MV of gun rf.

below the space charge limit (i.e., below about $50 \mu\text{J}$ in the figure).

It is interesting to ask whether the dark regions in Fig. 12, which appear to correspond to higher QE, are due to chemical or structural (roughness) changes of the cathode surface. This was investigated by comparing white light images taken with normal-incidence illumination and at oblique (or grazing) incidence. The cathode images are shown in Fig. 16, with oblique incidence in (a) and normal incidence in (b), (c), and (d).

Since the cathode surface was machined using optical quality diamond turning, its surface is mirrorlike and spectrally reflects the obliquely incident light away from the camera, while raised or rough regions will randomly scatter light into the camera. Careful examination of images (a) and (b) indicates good correspondence between the normal-incidence dark regions and the oblique image bright areas. It appears the dark regions are associated with higher QE (see Fig. 12), which in turn correspond to bright areas under oblique illumination (see Fig. 16). Therefore it is likely that the regions of increased QE are due to surface roughness produced by the laser plus rf processing, rather than by the laser removing chemical impurities. The enhanced surface roughness combined

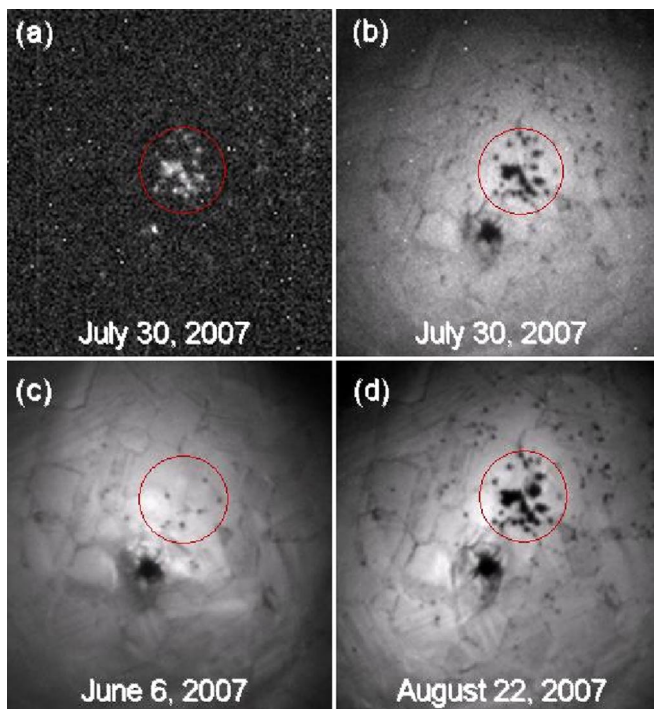


FIG. 16. (Color) White light images of the cathode taken using oblique illumination (a) and using normal-incidence illumination (b), both taken on July 30. Normal-incidence images taken on June 6 (c), early in the run, and again on August 22 (d), at the end of the run, clearly show the cathode image evolution. The camera views the cathode at normal incidence in all cases and the red circles show the nominal 1.3-mm diameter laser illumination area.

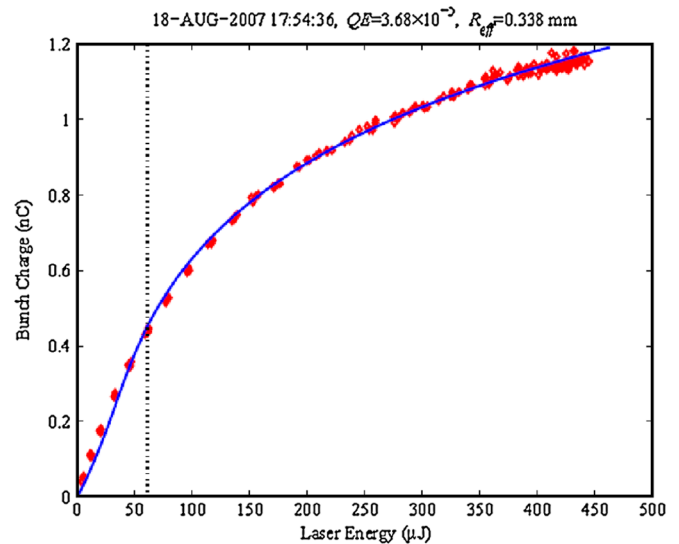


FIG. 17. (Color) The measured bunch charge vs laser energy fit with an analysis for the QE and the space charge limit. The QE in this case was 3.7×10^{-5} and the effective transverse radius is 0.34 mm rms.

with the high rf field lowers the work function via the Schottky effect, which increases the QE. Further study is needed to verify this hypothesis.

The QE history shown in Fig. 13 is an approximation based upon the charge emitted at the rf phase which produces the maximum cathode field (approximately 90 degS from the zero-field phase), and normalized to the laser energy. A more precise measurement is given in Fig. 17, where the charge is given as a function of the laser energy at the laser-rf phase of 30 degS from the rf zero crossing. This data was taken near the end of the run when stability had improved and the bunch charge had risen beyond 1 nC. The linear portion at low laser energies gives the quantum efficiency and the onset of the space charge limit is indicated by the rollover of the curve from this linear dependence. The space charge limit is quantified by an effective transverse rms radius assuming a Gaussian distribution [13,14].

VI. rf SYSTEMS

The LCLS injector rf system [15] consists of 6 stations, 5 of which operate at S-band (2.856 GHz) and use standard SLAC modulators and klystrons, and one which operates at X-band (4th harmonic at 11.424 GHz) using a modified SLAC modulator and an XL-4 klystron [16]. With the exception of the LIS station (see Fig. 1), a separate klystron is used to drive each accelerating structure, with no rf pulse compression. For the LIS section, a single station with SLED pulse compression [17] drives three structures. The S-band accelerators are standard SLAC structures approximately 3 meters long with the L0a and L0b structures (see Fig. 1) modified for dual feed rf input to mini-

mize transverse dipole fields at these low energies. The X-band system (L1X) uses a 60-cm duel-feed structure test accelerator, and the transverse rf deflector cavity (TCAV) in the injector is an old (1960's) 0.55-m long transverse structure at S-band.

Each station has an rf source controlled by an IQ modulator located in a phase and amplitude controller, PAC, chassis. The IQ modulator is driven by two 102-Ms/s arbitrary waveform generators. This allows a controlled power ramp to reduce rf gun reflections, and direct production of the phase flip required for SLED operation. Signals from couplers on the structure inputs and outputs are down mixed in a phase and amplitude detector module, PAD, with a 2830.5-MHz local oscillator (LO) to a 25.5-MHz intermediate frequency (IF), then digitized at 102 million samples per second (Ms/s), measuring phase and amplitude during the pulse.

The measured phase and amplitude from the PAD is used in a feedback loop to control the output rf of the PAC. The feedback loop operates on a Versa-Modular Eurocard based input/output controller in EPICS at the full machine rate—currently 30 Hz, but to be increased to 120 Hz in the future. The set-points for some of the rf feedback loops are controlled at a lower rate by beam-based measurements, or by other high level applications.

The various nominal rf phase and amplitude set-points (at 1 nC), their required short-term stability tolerances, and their measured stability are listed in Table III. The measured values are read using the rf PADs over 20 seconds, with feedback loops active. Variations over longer time scales will be mitigated with the use of beam-based feedback systems as described in [18]. The short-term stability tolerances for the injector have been achieved for each rf

TABLE III. Charge, rf phases (with respect to crest), and amplitudes, showing nominal settings, rms short-term stability tolerances, and achieved rms values for the LCLS injector. The measured values are an rms over 20 seconds at a 10-Hz sample rate.

Parameter	Nominal setting	rms tolerance	rms measurement	rms unit
Charge	1 nC	2	1.1	%
Laser phase	30°	0.5	0.2	degS
Gun phase	0	0.1	0.03	degS
Gun amplitude	6.0 MV	0.1	0.02	%
L0a phase	0	0.1	0.04	degS
L0a amplitude	57 MV	0.1	0.02	%
L0b phase	-3°	0.1	0.08	degS
L0b amplitude	72 MV	0.1	0.03	%
L1S phase	25°	0.1	0.09	degS
L1S amplitude	149 MV	0.1	0.06	%
TCAV phase	±90°	0.5	0.3	degS
TCAV amplitude	1.0 MV	0.5	0.2	%
LIX phase	-160°	0.5	0.3	degX
LIX amplitude	20 MV	0.5	0.2	%

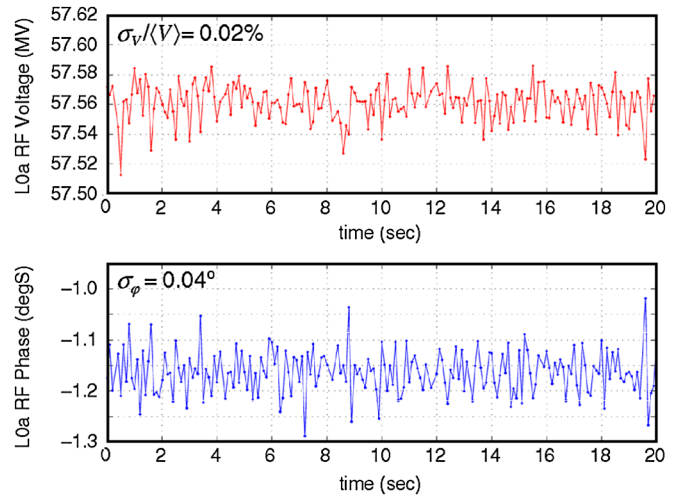


FIG. 18. (Color) The rf amplitude (top) and rf phase jitter (bottom) of the L0a rf section measured over 20 seconds at a 10-Hz sample rate (feedback active).

system as listed in the Table and shown for the L0a system in Fig. 18. These levels were only achieved in the last few weeks of the run.

A typical phase scan is shown in Fig. 19, which is used to find the rf crest phase by measuring the horizontal beam position on a BPM after a bend magnet, typically providing a phasing resolution of $<0.1^\circ$.

The L1S phase is operated about 25° off crest to install a linear energy chirp (energy-time correlation) along the bunch for compression in the BC1 chicane. The L1X phase is operated at about 20 MV, near the decelerating crest (-160°) and is used to remove the 2nd-order chirp induced by L1S, and also to add more linear chirp. It decelerates the beam from 269 to 250 MeV just prior to

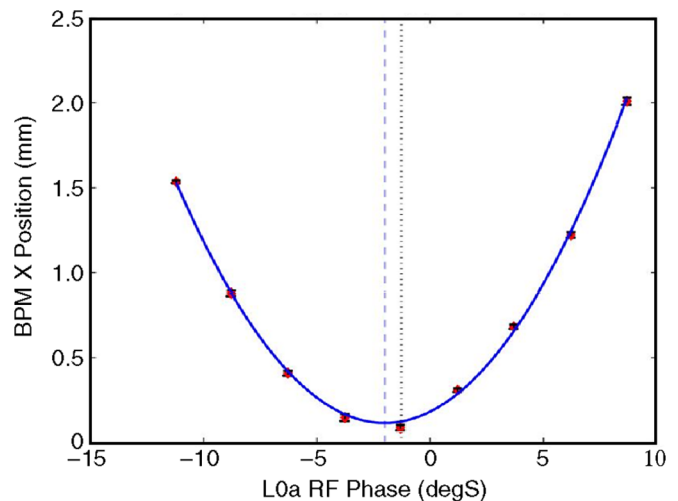


FIG. 19. (Color) An L0a rf phase scan used to find the rf crest phase by measuring beam position on a BPM after a bend magnet. The typical phasing resolution using 5 shots per phase setting and a parabolic fit is $<0.1^\circ$ rms.

compression in BC1. The other rf phases are operated at or very near the accelerating crest, except the laser-to-gun phase (30°) and the transverse deflector ($\pm 90^\circ$), which operates at either zero crossing, but only when needed as a diagnostic.

The rf reference system is located in a new temperature controlled room, the rf-hut, located in the linac gallery above the injector vault. Temperature stability of the rf system is further improved by running temperature stabilized water through the rf chassis. All of the critical rf signals are measured with phase and amplitude detectors, PADs, located in the rf-hut, which encloses a tunnel penetration leading to the linac enclosure 25 feet below. Phase stable $\frac{1}{2}$ -inch Superflex coaxial cable is run from the PADs down the penetration and into the linac tunnel where it connects to a coupler on the rf device of interest. The cables, located in a temperature stable environment, are expected to vary by less than 1-ps in length after the linac housing has reached its nominal temperature, typically several weeks after operations have begun.

The rf in the distribution system is referenced to the 476-MHz rf in the linac 3-km main drive line. The 476-MHz rf is multiplied up to 2856 MHz, which is used to drive the S-Band klystrons. The 2856-MHz rf is divided by 112 to generate the 25.5-MHz IF frequency and this is multiplied by four to generate the 102-MHz clock frequency used for the ADCs and DACs. The PADs use a 2830.5-MHz LO generated from the 2856-MHz reference and the 25.5-MHz IF frequency. The 2830.5-MHz is used as a local oscillator reference to measure critical rf signals against.

The rf beam phase monitor cavities tuned at 2805 MHz are 25.5 MHz below the LO frequency. Use of this frequency, rather than 2856 MHz, suppresses the signal due to dark current by 47 dB. The first beam phase cavity is located between the L0a and L0b structures. The second beam phase cavity is placed just after BC1. The beam phase, cavity frequency, and bunch current are calculated from the PAD data and made available to the control system (see example in Fig. 37).

VII. BEAM DIAGNOSTICS

Many of the beam diagnostic locations are shown in Fig. 1. Transverse beam profiles are measured using seven $1\text{-}\mu\text{m}$ thick aluminum OTR (optical transition radiation) screens; seven $100\text{-}\mu\text{m}$ thick Ce-doped YAG (yttrium aluminum garnet) screens for use at low energy where OTR provides limited light. The light from both YAG and OTR screens is detected with a common enclosed optical assembly consisting of a calibration reticle, a set of two insertable neutral density filters, a telecentric lens, and a 12-bit resolution megapixel CCD camera with digital output. The OTR screen resolution is approximately $12\text{-}\mu\text{m}$ per pixel.

There are also seven wire scanners (x and y), which require multiple beam shots, but are minimally invasive.

These are $20\text{-}\mu\text{m}$ thick tungsten wires to accommodate $\geq 40\text{-}\mu\text{m}$ rms beam sizes. The stepper motors are referenced with linear variable differential transformers with $2\text{-}\mu\text{m}$ accuracy. The raw profiles from a scan are typically taken from fast ion chamber readings and can be corrected for charge and beam position jitter by simultaneously acquiring data from nearby BPMs. In addition, the injector includes 22 stripline BPMs with $5\text{-}\mu\text{m}$ resolution; six beam current toroids; and two Faraday cups (one nonfunctional).

Finally, two transverse (vertical) S-band rf deflectors [19] are included to allow time-resolved beam measurements, such as the time-sliced emittance, slice energy spread, and absolute bunch length. The rf deflectors “streak” the bunch vertically across a nearby OTR screen so that the vertical axis becomes the time axis (Fig. 20, center). The time scale is accurately calibrated in degrees S-band (2.856 GHz) by scanning the rf deflector phase (e.g., ± 7 degS) and recording the vertical beam centroid motion on the screen. Longitudinal phase space is also monitored by using the deflector with a screen after a bend (Fig. 20, right). The first, 0.55-m long deflector (~ 1 MV peak) is located in the injector, while a 2.4-m long rf deflector (~ 25 MV peak) is located near the end of the linac (moved to a location just beyond the BC2 chicane in late 2007).

The projected emittance (integrated over the full bunch length) can be measured at 135 MeV using three OTR screens (see Fig. 21), three wire scanners, or scanning a quadrupole magnet current while using the middle screen or wire (i.e., a “quad-scan”). If the transverse cavity is switched on, a quad-scan on the middle screen produces the time-sliced horizontal emittance with picosecond temporal resolution (see Fig. 28).

Beyond BC1 is a second emittance diagnostic station at 250 MeV with three wire scanners (see Fig. 22) and an OTR screen to allow a quad-scan. The quadrupole magnet for this scan is separated from the screen by only a 2.5-m long drift, allowing a very simple projected emittance calculation. In addition, the time-sliced vertical emittance can be measured at the center of the chicane, where the time resolution is provided by the large energy chirp and dispersion. In this case the scanned quadrupole magnet is

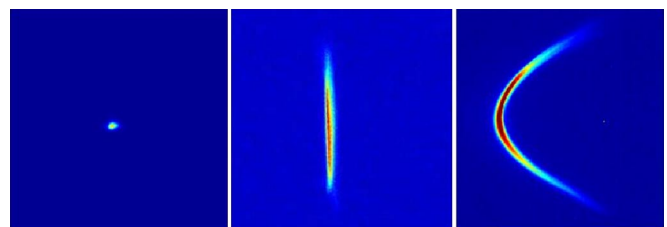


FIG. 20. (Color) OTR image with rf deflector “OFF” (left) and “ON” (middle), to measure slice emittance. YAG screen after a bend (right) with deflector ON, reveals longitudinal phase space directly on the screen.

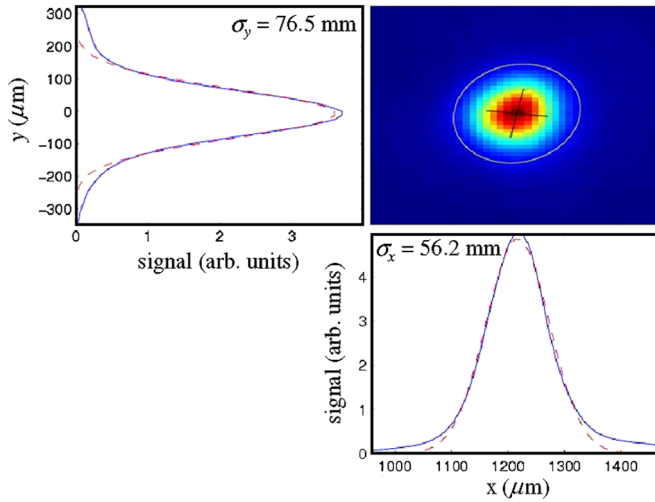


FIG. 21. (Color) Measured beam profile in both planes on the “OTR2” screen (2nd OTR in Fig. 1) at 135 MeV with 56 μm and 76 μm rms sizes in x and y , respectively. Gaussian profiles (red-dashed) with the same rms are overlaid here for convenient comparison.

4 m upstream of the screen, with one quadrupole and two dipole magnets intervening, requiring careful optical modeling for an accurate slice emittance measurement.

The wire scanners presently exhibit some fast vibration during the scan which might be driven by the stepping motor. The vibration may be the wire itself or the scanner assembly, and the amplitude is quite sensitive to the scanning speed but can be minimized by choosing the speed. The beam size results, however, can be corrupted by this effect and various solutions are being investigated.

The bunch length is monitored using two nonintercepting diagnostics after BC1. One monitor, referred to as *BL12*, incorporates a ceramic gap into the beam pipe

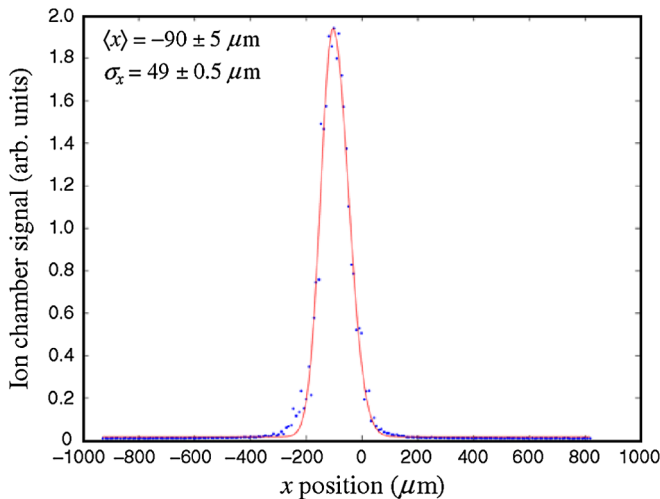


FIG. 22. (Color) Measured horizontal beam profile using 2nd of three wire scanners after BC1, showing a 49- μm rms size based on a Gaussian (red) fit. The signal is a fast ion chamber downstream of the wire.

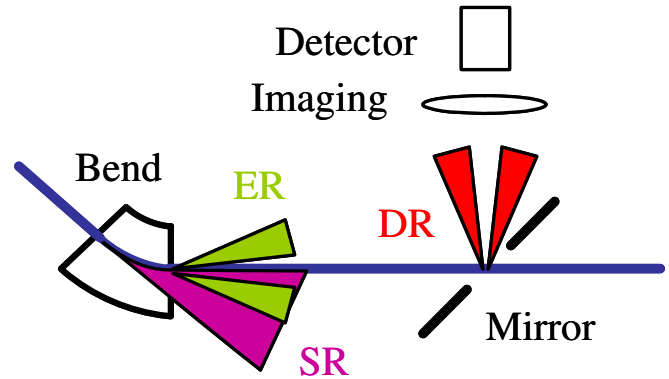


FIG. 23. (Color) Radiation source viewed by bunch length monitor *BL11*. The pyroelectric detectors measure primarily coherent edge radiation of the final BC1 bend, reflected into the detector by an insertable mirror with a 0.6-inch diameter hole to pass the electron beam.

downstream of the compressor. The microwave radiation generated by the short bunch wakefields is transmitted through the ceramic and is detected by two fast waveguide-coupled diodes which are sensitive to 100 and 300-GHz radiation. Once calibrated against the bunch length measurements using the transverse rf deflector, these signals are used to feedback the LIS rf phase and regulate the bunch length after BC1. The energy is simultaneously held constant using the BPM in the chicane by also controlling the LIS rf amplitude.

A second bunch length monitor, *BL11*, located immediately after the last BC1 dipole magnet, primarily measures the coherent edge radiation generated by the short bunch as it passes through the edge of the dipole. Synchrotron radiation from the bend itself and diffraction radiation from an insertable annular mirror, used to extract the edge radiation, is also detected. An optical imaging system directs the edge radiation onto a pair of pyroelectric detectors. Its general layout is given schematically in Fig. 23.

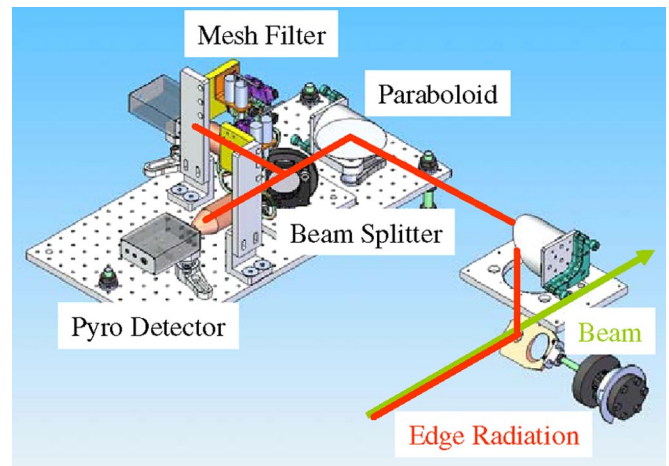


FIG. 24. (Color) A computer generated drawing of the *BL11* bunch length monitor system following BC1.

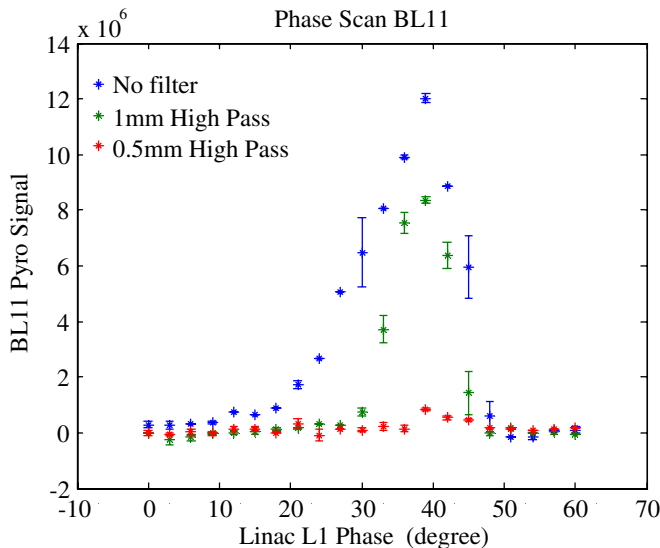


FIG. 25. (Color) Response of pyroelectric detectors (arbitrary scale) as a function of the L1S rf phase (rf section before BC1). A phase of zero is on-crest and a positive phase compresses the bunch length. The plot is shown for: (1) no wavelength filter (blue), (2) a 0.5-mm high-pass filter (red), and (3) a 1-mm high-pass filter (green).

The *BL11* device is more commonly used to drive the L1S rf phase feedback.

The design of the *BL11* bunch length monitor is shown in Fig. 24. The radiation is split into two detectors, each with two different sets of high-pass filters (1.0-mm and 0.3-mm for pyro-1, and 0.5-mm and 0.16-mm wavelengths for pyro-2). These can be inserted to select the wavelength of interest. The response of these detectors as a function of the L1S rf phase is plotted in Fig. 25 for the case with: (1) no filter, (2) a 0.5-mm filter, and (3) a 1.0-mm filter. Increasing the L1S rf phase increases the bunch energy chirp resulting in more compression (shorter bunch) after BC1, until the bunch is overcompressed (i.e., longer) at about 40 degS here.

VIII. MEASUREMENT AND ANALYSIS OF TRANSVERSE EMITTANCE

The LCLS injector transverse emittance at 135 MeV is most typically measured using an OTR screen with a quadrupole-scan. For the projected emittance, the quadrupole which is varied in gradient (scanned) is separated from the screen by only a 2.2-m long drift, allowing a very simple calculation. The screen images are acquired with a digital CCD camera; background subtracted, and analyzed using a variety of methods to eliminate spurious results due to pixel noise and long distribution tails. The online software allows x - and y -plane image projections to be analyzed simultaneously extracting the rms beam sizes. This is based on several optional methods, including: (1) rms of entire profile, (2) Gaussian fit, (3) asymmetric

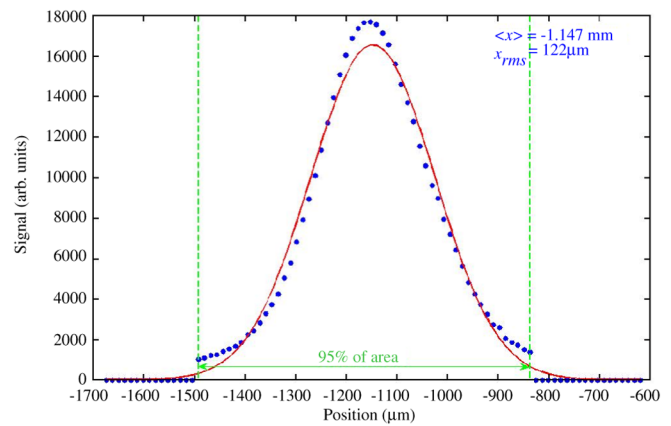


FIG. 26. (Color) Example measured horizontal beam profile ($\sigma_x \approx 122 \mu\text{m}$) from OTR screen at 135 MeV with “5% area-cut” applied, eliminating the tails. (A red Gaussian curve with the same rms is overlaid simply for comparison.)

Gaussian fit, (4) 5% amplitude-cut, and (5) 5% area-cut (i.e., charge-cut).

The emittance results reported here consistently use the 5% area-cut technique. In this method the background subtracted image is integrated in the two transverse dimensions over the region of interest (ROI) and the level corresponding to 2.5% of each x and y area-integrated projection is found on each side of the distribution. The rms beam size for the projections above these thresholds (see Fig. 26) is used to compute the emittance. Space charge forces are not included in the emittance analysis and should have no significant impact at these energies.

An example of the emittance results using the 5% area-cut analysis is given in Fig. 27 (top: x ; bottom: y). The plots on the left side show the rms beam size as a function of the varying quadrupole field, with fitted curve overlaid. The beam emittance, Twiss, and matching parameter (ξ , see below), as well as the goodness of fit (χ^2/NDF) are listed on the plot. The dashed green ellipses at right represent the reference (design) phase space of the x and y -planes at the OTR screen for the nominal quadrupole field. The solid black ellipses reflect the measurements. The straight dashed lines represent the measured beam size at each quadrupole setting, transformed and rotated to the reference phase space. Ideally (i.e., when $\chi^2 = 0$) the straight lines will all intercept the measured (fitted) ellipse precisely at their tangent points.

The statistical errors of the various measured beam parameters are estimated by acquiring each image multiple times (typically 5–10) for each quadrupole setting. From the multiple projections, the average beam size is taken, and in addition, the standard error is used as a weighting factor in the least-squares fit. The standard error is defined as the standard deviation of the beam size values, divided by the square root of the number of repeated measurements. This statistical beam size error is then propagated to the emittance result. Such a treatment may tend to under-

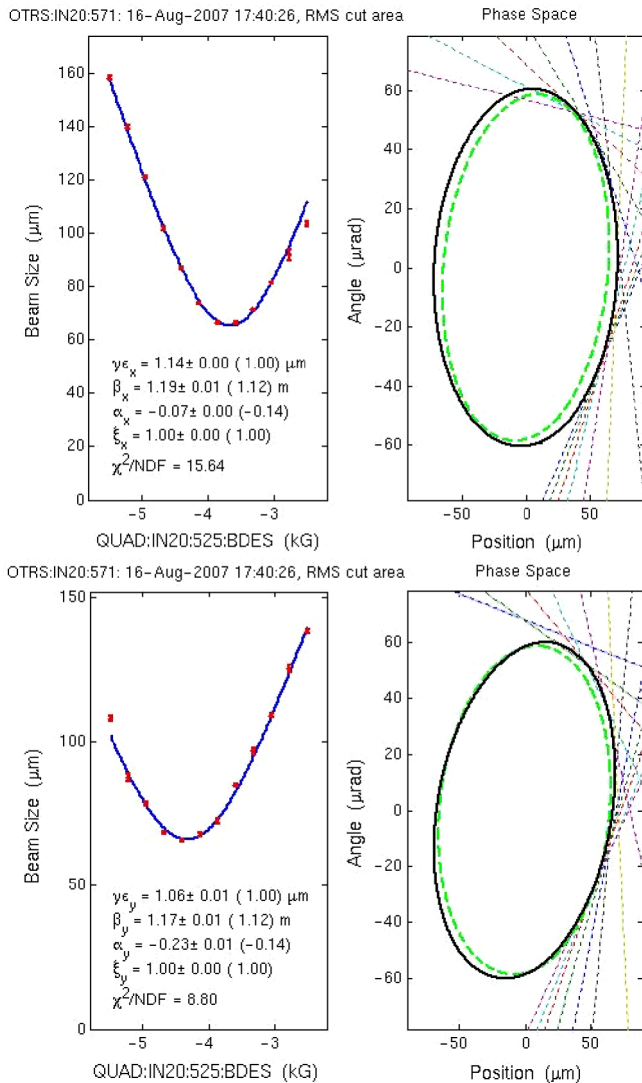


FIG. 27. (Color) Projected normalized x (top) and y (bottom) emittances measured for a 1-nC, 100-A bunch at 135 MeV ($\gamma\epsilon_x \approx 1.14 \mu\text{m}$, $\gamma\epsilon_y \approx 1.06 \mu\text{m}$). The beta-matching parameter, $\xi_{x,y}$ (see below) is 1.00 in x and y , showing an ideally matched beam to the design Twiss functions.

estimate the error since beam size variations during the full measurement may not adequately be incorporated into the error. The beam size is quite repeatable over the few seconds at each quad setting, but may drift appreciably more during the full scan. There are no estimates included for systematic errors anywhere in this report, since they are not yet quantified. In fact, the choice of the ROI may be one such source of systematic error. In Fig. 21 some beam tails are seen to be cut by the choice of ROI. This may tend to bias the reported emittance toward smaller values. This source of systematic error has not been studied in any detail yet, but should not much alter the *core* emittance value. The *core* rms emittance may therefore actually represent somewhat less than 95% of the charge, as mentioned below in Sec. IX.

The electron bunch length, slice emittance, and slice energy spread are also measured on this same OTR screen (2nd OTR in Fig. 1) with the transverse rf deflector switched on, applying the same 5% area-cut analysis method to the data. Such a time-sliced horizontal emittance measurement is shown in Fig. 28 at 1-nC of charge and a 1.3-mm cathode spot diameter and 10-ps FWHM electron bunch length (100 A, see Fig. 38). The slice emittance is well below $1.0 \mu\text{m}$ in the core and tail of the bunch (left side). Here the bunch has been binned into 12 slices (~ 1.7 ps per slice) and the horizontal emittance calculated for each slice (data connected with cubic spline). This measurement is also quite reproducible.

Also shown is the beta mismatch amplitude parameter (ξ) taken with respect to the design Twiss parameters. The definition of this matching parameter is

$$\xi \equiv \frac{1}{2}(\beta\gamma_0 - 2\alpha\alpha_0 + \gamma\beta_0) \geq 1, \quad (1)$$

where β , α , and $\gamma(\equiv [1 + \alpha^2]/\beta)$ are the measured Twiss functions of the beam, and the subscripted quantities refer to their design values. The beam is matched to the design when $\xi = 1$, and imperfectly matched when $\xi > 1$. Careful adjustment typically allows $1.00 < \xi < 1.05$ in each plane. Note that the slice emittance measurement at 135 MeV scans a different quadrupole magnet than for the projected emittance. This choice maintains the large vertical time streak on the screen. The scanned magnet is separated from the screen by 2.6 m, with one more intervening quadrupole magnet, requiring more careful optical modeling for the slice emittance calculation.

The time-sliced emittance is typically less than the projected emittance. Some of this inequality is explained

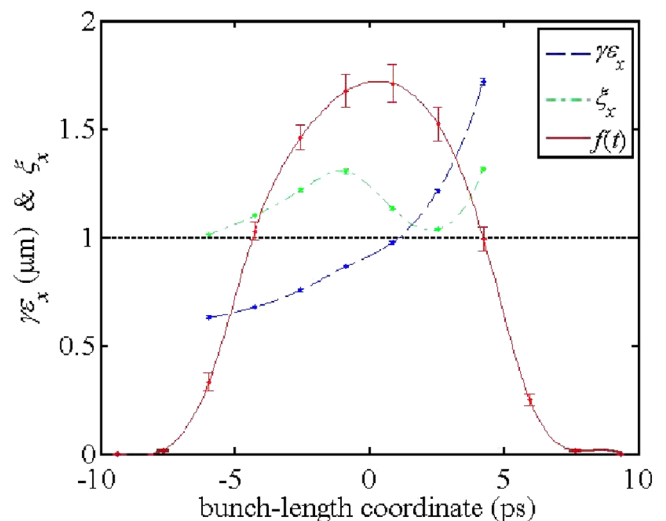


FIG. 28. (Color) The time-sliced horizontal emittance ($\gamma\epsilon_x$ in blue), mismatch parameter (ξ_x in green), and temporal distribution [$f(t)$ in red, on arbitrary scale], for a 1-nC, 100-A bunch at 135 MeV, with emittance values $< 1 \mu\text{m}$ in the beam core and tail (bunch tail at left).

in Fig. 29 (left), where the variations in the horizontal position along the vertical coordinate (i.e., the time coordinate with rf deflector switched on) lead to an increased projected emittance above the slice value.

The time-sliced energy spread is also measured with the rf deflector, by streaking the beam across a YAG screen just downstream of the 35-degree bend magnet in the 135-MeV spectrometer (Fig. 29, right). With the 880-mm horizontal dispersion here, the slice energy spread (before compression) is measured at <6 keV rms at 150 pC in the core of the beam (a $40\text{-}\mu\text{m}$ rms core x -size). The uncorrelated (slice) energy spread may actually be smaller since the screen is resolution limited at $30\text{--}40\ \mu\text{m}$ with an estimated 0.2-m horizontal beta function and $1\text{-}\mu\text{m}$ emittance.

Many measurements have been made using OTR screens and wire scanners, which confirm the normalized rms emittance level at about $1.2\ \mu\text{m}$ in both transverse planes at a bunch charge of 1 nC, electron energy of 135 MeV, and peak current of 100 A. The various emittance measurements at 1 nC extend from $1\ \mu\text{m}$, and on occasion up to 1.5 microns, with an undetermined source of variation. The bunch length ($10\text{--}11$ ps) is somewhat larger than its design level of 9 ps FWHM, which produces a peak current of $90\text{--}100$ Amperes. The long bunch is likely due to a small laser spot size. Figure 30 shows the horizontal and vertical projected emittance at 135 MeV and 0.7 nC charge using a quad-scan and OTR screen measured 30 times over almost 8 hours, averaging $\gamma\epsilon_x \approx 0.95\ \mu\text{m}$ and $\gamma\epsilon_y \approx 1.02\ \mu\text{m}$. Each emittance measurement requires only about 2 minutes and returns both planes.

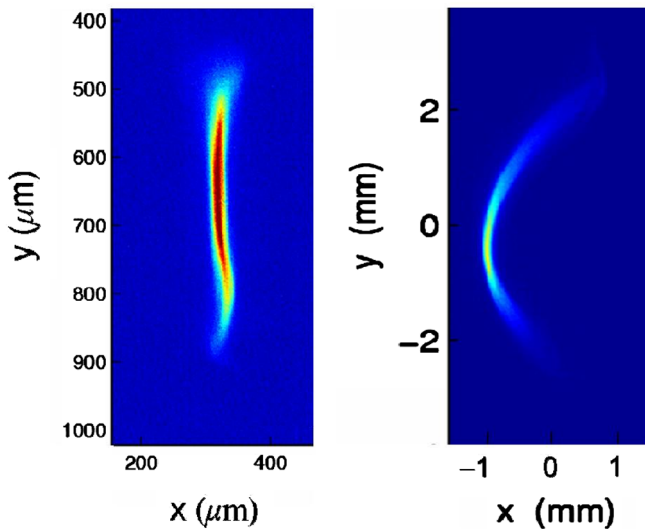


FIG. 29. (Color) Beam vertically streaked across OTR screen (left) and YAG screen (right) using rf deflector (bottom is bunch tail). At left, variations in horizontal position along the vertical coordinate (time) lead to an increased projected emittance above the slice. At right, a YAG screen after the 35-deg spectrometer bend at 135 MeV reveals a slice (intrinsic) energy spread of <6 keV rms.

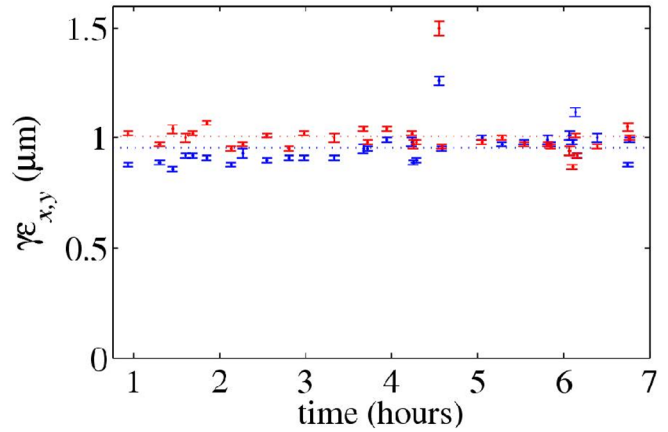


FIG. 30. (Color) Horizontal (blue) and vertical (red) projected emittance at 0.7 nC, 135 MeV, and 70 A, measured continuously over almost 8 hours. A sudden klystron error caused the spike at 4.5 h.

The variations in emittance are larger over longer time scales, especially at the full bunch charge of 1 nC. It is not uncommon to observe daily variations from 1.1 to $1.4\ \mu\text{m}$ at 1 nC, with $1.2\ \mu\text{m}$ typically achieved after some brief reoptimization, such as a small gun-solenoid adjustment (Fig. 31) or laser spatial profile correction.

It is important to stress that these rms emittance values are measured over the full bunch length (time-projected), but the rms analysis includes only 95% of the core charge, as described above. Measurements which use an rms from the full transverse distribution are much more sensitive to baseline noise and weak charge tails, and typically report larger emittance levels closer to $1.5\ \mu\text{m}$ and larger.

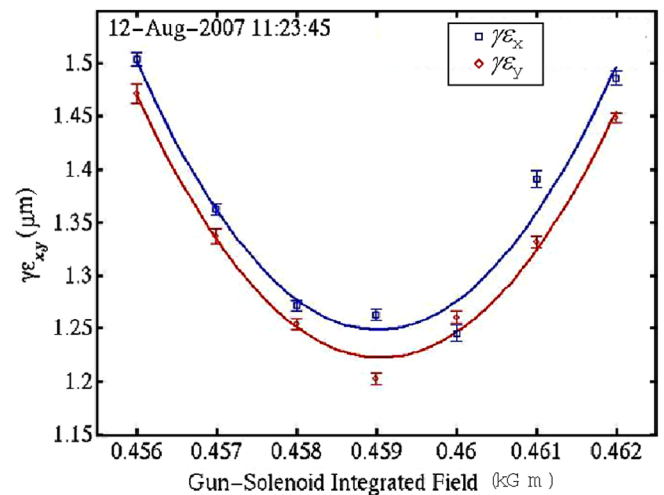


FIG. 31. (Color) Gun-solenoid field scan to minimize x (blue) and y (red) projected emittance at 135 MeV and 1 nC with a gun exit electron energy of 6.0 MeV. More typically the two minima are not so well aligned.

IX. BEAM TRACKING SIMULATIONS

Simulations of the beam emittance measurement were performed [20] using the IMPACT particle tracking code [21]. A quiet-start generator, based on a Halton sequence of numbers, is used to build the initial particle distribution exiting the cathode. The generated 6D distribution was based on the 3D projections of the measured emission distribution early in the run and uses Gaussian transverse momentum distributions with rms values such that the thermal emittance is $0.6 \mu\text{m}$ per millimeter of laser spot radius (hard edge) on the cathode. The longitudinal momentum used is $1 \text{ eV}/c$.

The transverse photoelectron emission distribution is frequently measured at low charge with a point-to-point imaging of the cathode on a YAG screen located in the gun-to-linac section. Figure 32 (top) shows the particular emission profile used in these simulations. This image is taken with the laser iris closed such that the laser diameter is

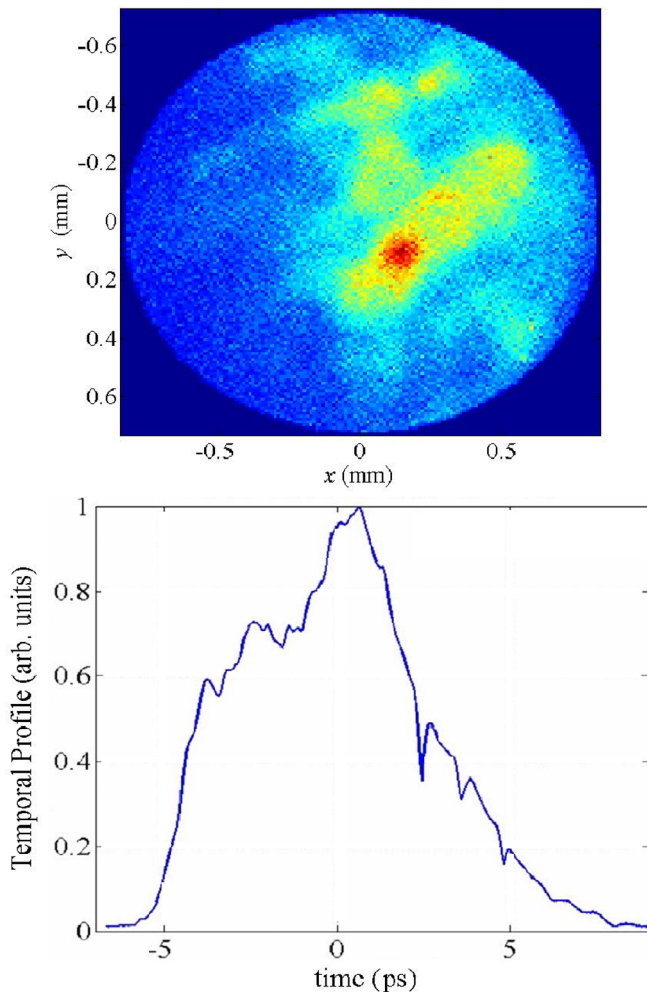


FIG. 32. (Color) Point-to-point image of cathode (top) at low charge ($\sim 20 \text{ pC}$) observed on the second YAG screen of the gun-to-linac section, and the cross-correlator temporal profile (bottom) with bunch head at right.

1.6 mm on the cathode. The longitudinal profile used in these simulations is shown in Fig. 32 (bottom) and is measured with the cross correlator. These particular distributions used in the simulations represent the beam quality at one particular time early in the commissioning run and are not necessarily representative of the best or average conditions. The Schottky effect, represented in Fig. 8, which increases (decreases) the longitudinal charge density at the tail (head) of the bunch with respect to the laser profile, was ignored in the simulations as its effect is of second order for this 6-ps FWHM long pulse. This realistic electron beam distribution was “accelerated” to 135 MeV and propagated to the OTR screen in a simulation of the quadrupole-scan technique. The simulated transverse profiles were analyzed with the same area-cut method used in the real data, but for various fractional cut levels.

The results of this analysis are summarized in Fig. 33, where the transverse emittance values are plotted as a function of the percentage area-cut at 1 nC. The higher y-plane emittance results from the asymmetry of the initial electron distribution and is, at times, typical of the emittance asymmetry observed in the measurements.

Simulations were done both with 200 k particles and 4 million particles, with x - y - z meshing of $32 \times 32 \times 32$ and $128 \times 128 \times 64$, respectively. More structure was visible on the transverse profiles for the 4M particles, but the emittance curves were similar to that with 200 k particles.

Comparing the measured emittances of Fig. 27 with the curves in Fig. 33 indicates that a fractional cut of 8%–9% would result in better agreement with simulation, whereas the measurements use a 5% area-cut. It is likely that a few percent of the measured distribution is lost in the image processing. This discrepancy is relatively small, and at

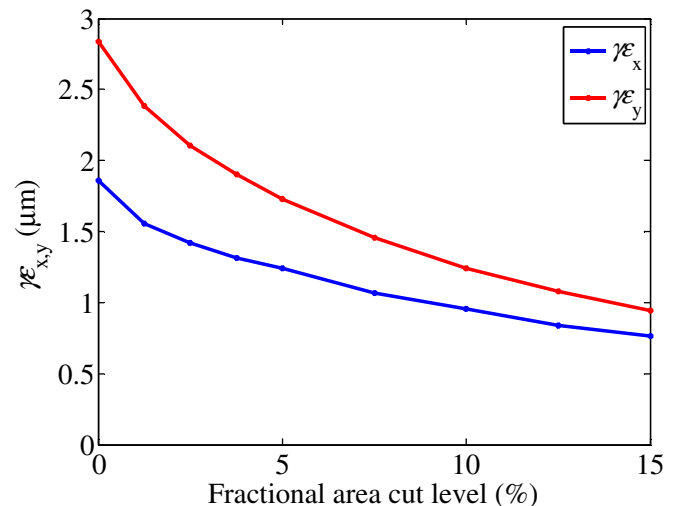


FIG. 33. (Color) Simulations of measured emittance, using the measured cathode emission and laser temporal profiles, as a function of the fractional area-cut levels. The bunch charge is 1 nC in this simulation.

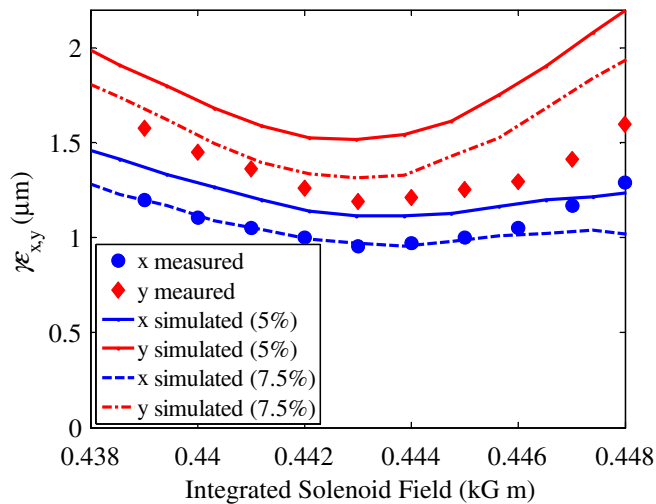


FIG. 34. (Color) Measured and simulated emittance vs gun-solenoid field. The measured emittances use a 5% area-cut, while simulations are shown for 5% and 7.5%. The bunch charge is 1 nC here and the gun exit electron energy is 5.75 MeV, explaining the lower solenoid field strength here than in Fig. 31.

worse may imply the measured emittances represent about 92% of the beam charge rather than 95%.

Simulations were also run of a gun-solenoid field scan, which is typically used to minimize emittance, and compared with measurements at 1 nC (see Fig. 34). Again, the measured emission profiles are used in simulation. With a 5% area-cut, the simulated emittance values are larger than the measured values, whereas a 7.5% area-cut allows better agreement in both planes. The emittance values, in measurement and simulation, are clearly quite sensitive to the presence of weak transverse tails, and therefore the precise area-cut level.

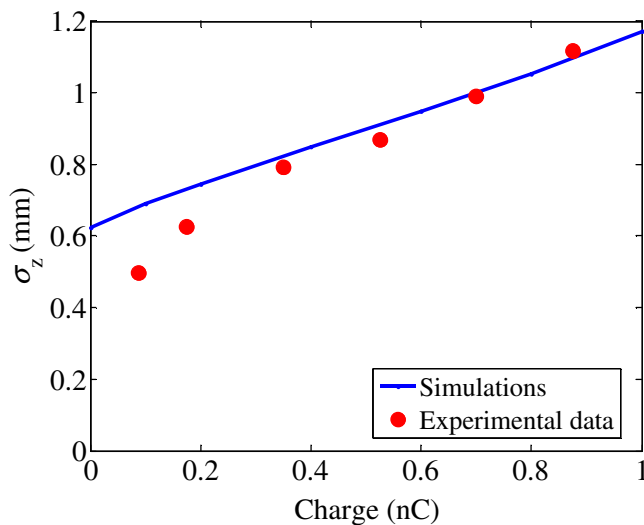


FIG. 35. (Color) The rms bunch length at 135 MeV versus bunch charge. Measured values are compared to simulations using a thermal transverse emittance of $0.6 \mu\text{m}$ per millimeter of radius and a 5-ps FWHM laser pulse.

The bunch length was also simulated versus charge and compared with measurements (see Fig. 35). These measurements were performed with an initial 5-ps FWHM laser pulse. Good agreement is obtained for most charge levels, except the two lowest. The rms bunch length of 1.1 mm at high charge is larger than the design value of 0.85 mm rms in large part due to the use of smaller laser diameter, 1.3 mm, instead of the 2-mm design level.

X. BUNCH LENGTH COMPRESSION

The LCLS injector includes a 4-dipole magnetic chicane (BC1) at 250 MeV as the first bunch compression stage (see Table IV). The 35-deg bend system at 135 MeV does not compress the bunch and the second compressor, BC2, will be located 360 m downstream at 4.3 GeV and installed in the fall of 2007. Nominally, the bunch is compressed by a factor of 4.5 in BC1, but in the extreme, with the X-band 4th harmonic rf switched ON (20-MV amplitude and phase set near decelerating crest) to linearize the energy chirp (see Fig. 36), the bunch can form a spike $<1 \mu\text{m}$ in rms length [22]. This is due to the very small uncorrelated (time-sliced) energy spread in the beam ($<6 \text{ keV}$ rms).

TABLE IV. Nominal BC1 compressor chicane parameters.

Parameter	Symbol	Value	Unit
Electron energy	E_0	250	MeV
Chirped rms energy spread	σ_E/E	1.6	%
Momentum compaction	$ R_{56} $	39	mm
Chicane total length	L_T	6.5	m
Bend angle per dipole	$ \theta $	4.97	deg
Effective length of each dipole	L_B	0.204	m
B1 to B2 drift (= B3 to B4)	ΔL	2.43	m
B2 to B3 center drift	ΔL_c	0.83	m
Field of dipole magnets	$ B_{y0} $	3.56	kG
Dispersion at chicane center	$ \eta_x $	230	mm
Translation adjust range	$ \Delta x $	0–300	mm
Relative field gradient tolerance	$ b_1/b_0 $	0.01 ^a	%
Relative sextupole field tolerance	$ b_2/b_0 $	0.05 ^a	%

^aB2 and B3 field components measured at a radius of 20 mm.

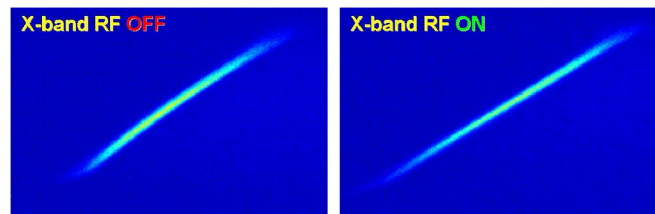


FIG. 36. (Color) Beam on the BC1 OTR screen with its large horizontal dispersion. The LIS rf phase is off crest by 25° . The first rf deflector is ON, and the X-band cavity is OFF at left, and ON (20 MV) at right, demonstrating proper X-band linearization of the energy chirp.

The chicane includes an OTR screen at its center (see Fig. 36), an adjustable pair of horizontal collimator jaws to remove energy tails (typically set wide open during operations), and a BPM used in a feedback loop to stabilize the BC1 electron energy. The chicane is built with a horizontal motorized translation stage (0–300 mm) to allow remote articulation. This keeps the beam in the dipole centers, permits a reasonable BPM and dipole aperture, and also allows the system to be straightened for 30-GeV non-LCLS linac operations.

The absolute bunch length after BC1 has been measured using a second vertical S-band rf deflecting cavity (LOLA), 2.4 meters long [19], with 25 MV of peak transverse voltage, located 900 meters downstream of BC1. This cavity functions as a robust, high-resolution streak camera. Bunch length measurements are shown in Fig. 37 at 1 nC, where the phase settings of the LIS and X-band rf sections (see Fig. 1) are both varied producing the rms chirped relative energy spread shown on the horizontal axis of this plot. The compression factor was also measured simultaneously by using the two beam phase monitor cavities, one upstream and one downstream of BC1, to measure the ratio of phase variations at each location as the phase of the drive laser was scanned. This measured compression factor is multiplied by the measured initial bunch length and plotted for clear comparison with the measured bunch length data.

The LOLA measurement is presently resolution limited by a phosphor screen at 14 GeV, which will be replaced during the fall 2007 installation period with a new OTR foil at 4.3 GeV. The poor agreement of the data in the range $\sigma_E/E > 4\%$ is not understood, but may be related to the

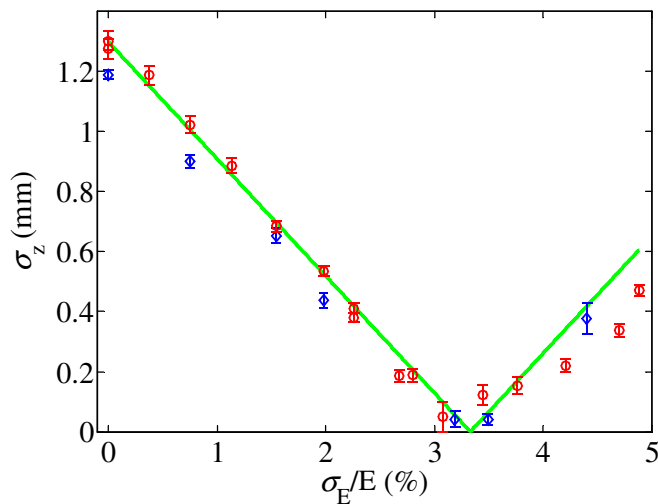


FIG. 37. (Color) The rms bunch length at 250 MeV after BC1, measured using the 2nd rf deflector (red circles), and the measured compression factor times the initial bunch length (blue diamonds), measured using two beam phase monitor cavities up and downstream of BC1. The (linear) calculated bunch length is also shown (green line).

poor screen quality. The rms chirped energy spread is about 30% larger than its design value due to a longer than nominal bunch length. The design value of the rms bunch length is 0.85 mm before BC1 and 0.20 mm after.

The 2.4-m LOLA cavity will be relocated to just after the BC2 in the fall of 2007, but during commissioning was installed near the linac end at 14 GeV. A shorter transverse cavity is also located upstream of BC1 (see Fig. 1) and used to measure the initial bunch length and longitudinal distribution (Fig. 38, top). The 14-GeV bunch was compressed to 170 μm rms in length (Fig. 38, bottom), and shorter, but with a resolution limit of about 100 μm rms.

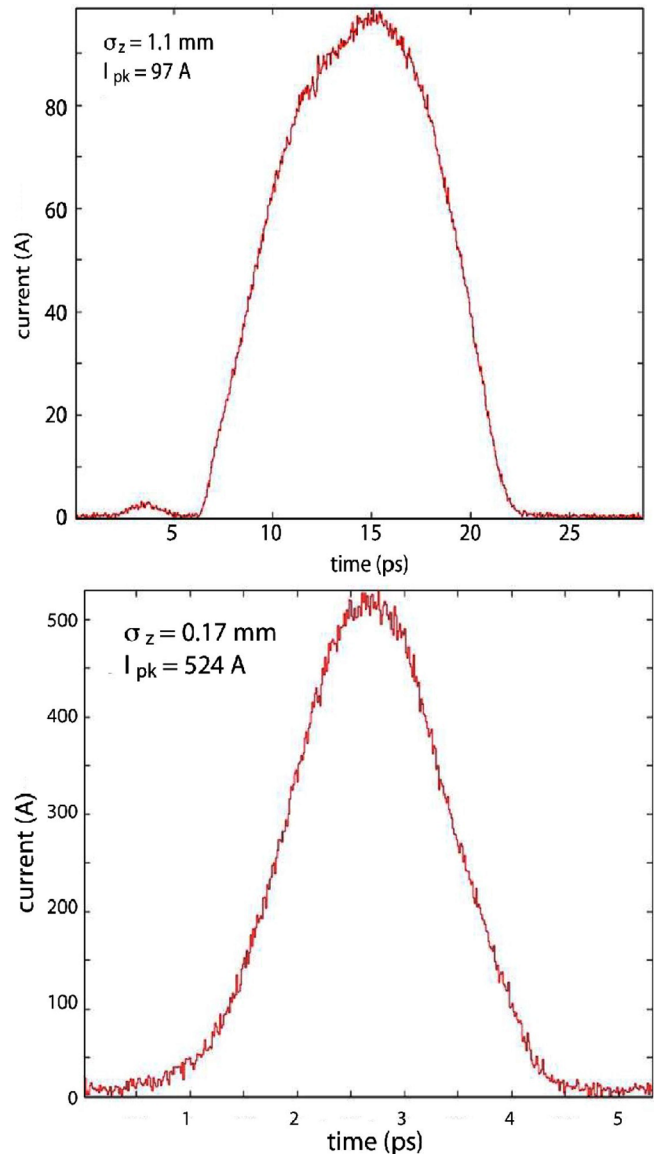


FIG. 38. (Color) Bunch length distribution measured using both rf deflectors. The first measurement is at 135 MeV (top: $\sigma_z \approx 1.1$ mm, $I_{pk} \approx 97$ A) and the second is at 14 GeV (bottom: $\sigma_z \approx 0.17$ mm, $I_{pk} \approx 520$ A), representing the bunch length before and after BC1 compression at 1 nC.

The BC1 dipole fields are unfortunately of poor quality, including a significant sextupole field and linear field gradient, generating large horizontal dispersion and emittance growth beyond BC1. The problem is magnified by the larger than nominal energy spread in BC1 due to the long initial bunch length. The linear dispersion after BC1 has been corrected using two small quadrupoles placed in BC1 for this purpose (see Fig. 39), but the remaining sextupole field limits the minimum horizontal emittance growth to about 40% ($\gamma\epsilon_x$ from $1.2 \mu\text{m}$ before BC1 up to about $1.7 \mu\text{m}$ after BC1). The BC1 dipole magnet poles are being shimmed and widened at present (fall of 2007).

In addition to the emittance growth generated by the large energy spread in the poor quality BC1 dipole fields, another source of horizontal emittance growth has been traced to the beam position in the small-aperture ($\sim 4 \text{ mm}$ radius) X-band rf structure, with its strong transverse wakefields. Figure 40 shows the horizontal emittance after BC1 as the beam's horizontal position is varied in the structure. The bunch charge is 0.7 nC , the bunch length is about 1 mm , and the BC1 chicane and X-band rf are both switched OFF here. The X-band structure was found to be 0.6-mm misaligned horizontally, which will be corrected in the fall of 2007, but the beam position must be carefully maintained here to within about $150 \mu\text{m}$. In addition, phase adjustments applied to the X-band rf have been observed to steer the electron beam horizontally. This effect is still being examined, but may be due to a structure yaw angle or coupler error.

Finally, the emittance can also be increased by the coherent synchrotron radiation (CSR) of a very short bunch in the BC1 dipoles. This effect is expected to be small

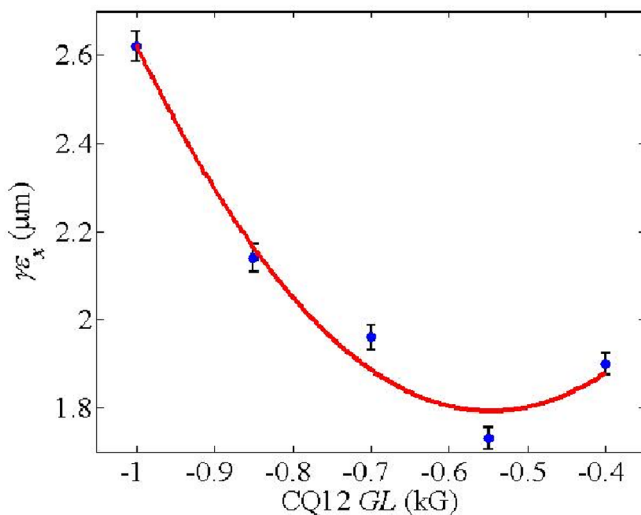


FIG. 39. (Color) Horizontal emittance at 250 MeV on OTR screen after the BC1 chicane, with nominal rf phasing, optimized by varying the length-integrated field gradient, GL, of the second BC1 dispersion quadrupole, CQ12. The emittance upstream of the BC1 was about $1.2 \mu\text{m}$.

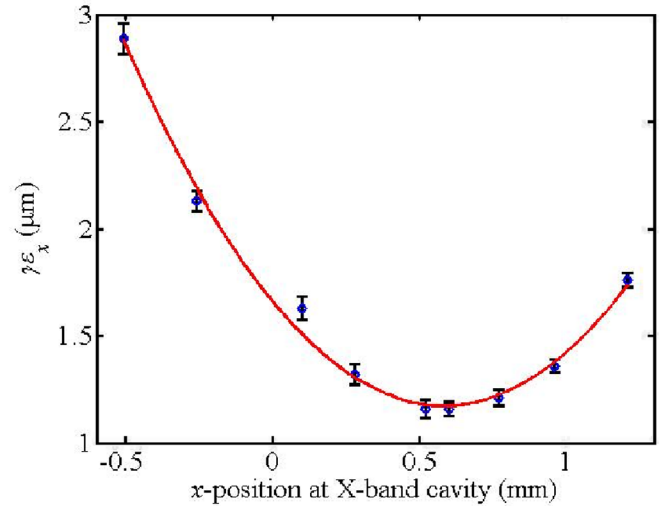


FIG. 40. (Color) Horizontal emittance at 250 MeV after BC1 as the beam's horizontal position is varied in the X-band rf structure. The charge is 0.7 nC , and the BC1 chicane and X-band rf are both switched OFF here. The LIS rf is at crest phase.

($< 2\%$ horizontal emittance growth) at the nominal post-BC1 bunch length ($200 \mu\text{m}$ rms) at 1 nC , but some attempt has been made to measure the CSR-induced growth by compressing the bunch length much shorter than nominal. These measurements were done at a charge of 300 pC , when the cathode QE was low, and are in reasonable agreement with calculations. This is reported in Ref. [22], where the bunch charge was described as 200 pC due to toroid calibration errors resolved only later. This measurement is difficult since the emittance measurements can be corrupted by the onset of coherent OTR from the beam screens as the bunch length is compressed toward its extreme (see below).

XI. UNEXPECTED PHYSICS

During beam emittance studies downstream of BC1, a strong enhancement of the optical signal from the OTR foils was observed with extreme bunch compression. The effect is illustrated in Fig. 41 where the BL12 microwave detector signals and the OTR optical signal, obtained by integrating the OTR image, are given vs the LIS rf phase in a semilog plot. Recall that increasing the LIS phase decreases the electron bunch length after BC1, where the LIS phase for nominal LCLS operation is 25 degS (when X-band rf is at -160 degX and 20 MV). The data shows the expected behavior for the two microwave signals. As the rf phase is increased, the 100-GHz diode signal responds first, followed by the 300-GHz diode near 35 degS . The 300 GHz signal saturates above 40 degS off crest. The BL11 bunch length monitor, described above, shows a similar result.

What is unexpected is the large increase in the OTR optical signal, rising at least an order of magnitude above

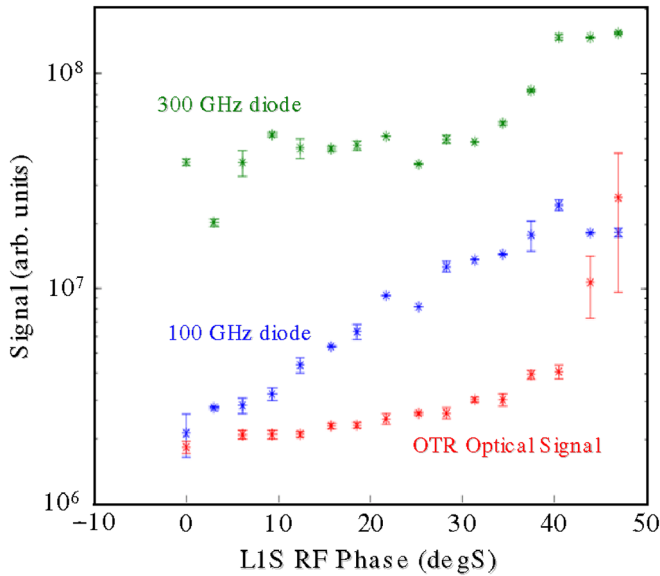


FIG. 41. (Color) The signals of the *BL12* microwave detectors at 100 GHz (blue) and 300 GHz (green), and the image-integrated OTR optical signal (red), as seen by a digital camera, are plotted (log scale) as functions of the LIS rf phase relative to the accelerating crest (at phase = 0). The increase in the OTR signal suggests the onset of COTR.

the unbunched signal although the bunch charge is constant. This behavior of the optical signal strength suggests the onset of coherent optical transition radiation (COTR) as the bunch develops a temporal spike with duration at optical wavelengths. The 6-keV rms upper limit slice energy spread at 250 MeV and the 39-mm R_{56} of the BC1 chicane suggest the spike may be 900 nm rms or less.

In addition to the large increase in the optical signal, the beam image greatly varies from pulse to pulse. This can be seen in the large variations of the beam profile measured

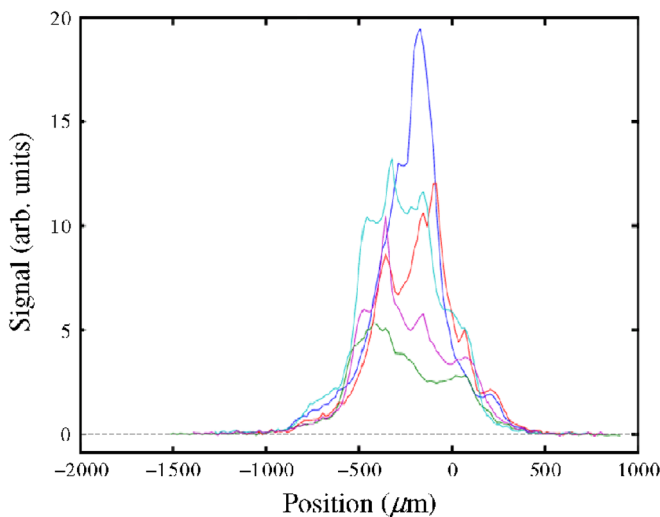


FIG. 42. (Color) OTR screen profile projections for five consecutive beam pulses when the LIS rf phase is set at 50 degS off crest, in conditions of extreme compression.

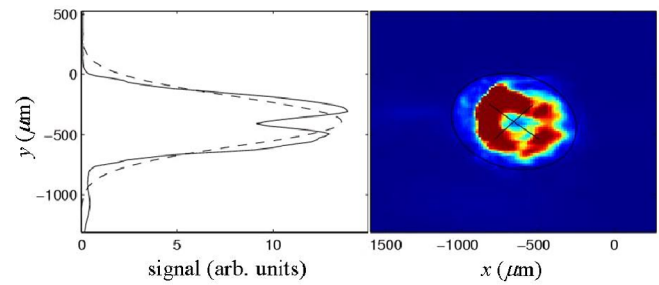


FIG. 43. (Color) An image of the COTR radiation after BC1 observed with extreme bunch compression.

with the OTR screen in these conditions of extreme compression. This is shown in Fig. 42, reflecting the statistical shot-to-shot variations in the projections of the images for a sequence of pulses. An adjacent wire-scanner profile (not shown) taken at the same time does not show these large profile variations. The OTR images themselves are quite striking, displaying chaotic patterns of random spots which can occasionally be organized into ringlike shapes. This ring effect can be seen in Fig. 43.

Another manifestation of this phenomenon is shown in Fig. 44. In this study, the OTR integrated optical signal for the foil is shown on the vertical axis, but in this case, BC1 is set to zero strength so as to produce no compression. The single quadrupole “QB” magnet between the two 17.5-degree dipoles (just upstream of LIS in Fig. 1) is varied in strength (horizontal axis) and the optical intensity varies with almost a Gaussian shape, centered exactly at the setting which makes the “dipole-quadrupole-dipole” bend system a perfect linear achromat. When the quadrupole magnet is set off this peak, the optical bunching is washed out by the x - z coupling of the nonachromatic bend

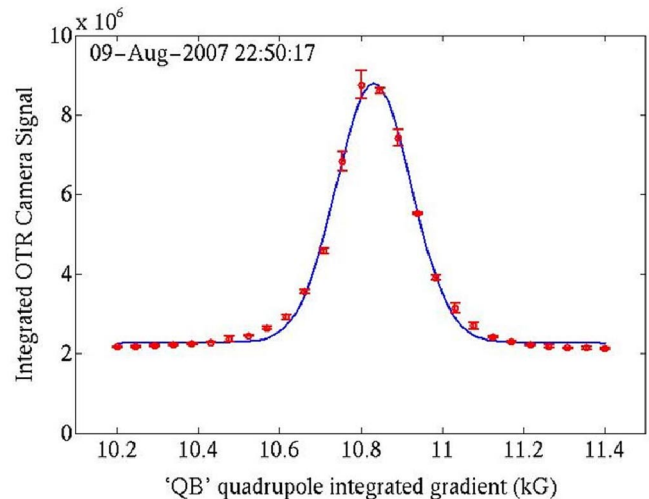


FIG. 44. (Color) The integrated optical transition radiation signal (background subtracted) as a function of the QB quadrupole magnet strength. The optical signal is a maximum at the quadrupole setting which makes the bend system a perfect linear achromat.

system, and the OTR signal settles down to its baseline, incoherent level. This phenomenon shows the likely presence of a microbunched beam at optical wavelengths generating strong COTR. The same effect has also been observed on a second OTR screen inside the BC1 chicane, but with the chicane bends switched off. Further study continues.

XII. SUMMARY

The required beam brightness for the LCLS has been demonstrated in the first phase of machine commissioning with the goal of a 1.2-micron emittance in a 1-nC bunch achieved. Most of the parameters described here only reached their design levels near the end of the commissioning cycle, in the last month or two of running after many lessons were learned and improvements applied. The challenge remains of preserving this exceptional beam brightness through the 1-km linac, including a second stage of bunch compression at 4.3 GeV in the BC2 chicane. This next phase of commissioning is planned for 2008, with the final challenge of 1.5-Å SASE FEL commissioning taking place in 2009.

ACKNOWLEDGMENTS

The authors would like to acknowledge the efforts of the entire LCLS project staff and the SLAC support groups for their continuing work in getting this machine designed, procured, fabricated, installed, and fully checked out. We especially acknowledge the operations group, the controls group, and the rf maintenance groups for their indispensable support during commissioning. This work was supported by the U.S. DOE Contract No. DE-AC02-76SF00515.

[1] R. B. Neal, *The Stanford Two-Mile Accelerator* (W. A. Benjamin, Inc., New York, 1968).

- [2] Z. Huang *et al.*, Phys. Rev. ST Accel. Beams **7**, 074401 (2004).
- [3] D. H. Dowell *et al.*, *Proceedings of the 2007 Particle Accelerator Conference, Albuquerque, NM* (IEEE, Piscataway, NJ, 2007), pp. 1317–1319.
- [4] C. Limborg-Deprey, D. Dowell, J. Schmerge, Z. Li, and L. Xiao, LCLS-TN-05-3, 2005.
- [5] L. Xiao, R. F. Boyce, D. H. Dowell, Z. Li, C. Limborg-Deprey, and J. Schmerge, *Proceedings of the 2005 Particle Accelerator Conference, Knoxville, TN* (IEEE, Piscataway, NJ, 2005), pp. 3432–3434.
- [6] D. H. Dowell *et al.*, in Ref. [3], pp. 1296–1298.
- [7] K.-J. Kim, Nucl. Instrum. Methods Phys. Res., Sect. A **275**, 201 (1989).
- [8] C. Limborg *et al.*, *Proceedings of the 2003 Particle Accelerator Conference, Portland, OR* (IEEE, Piscataway, NJ, 2003), pp. 3216–3218.
- [9] D. H. Dowell *et al.*, *Proceedings of the 2002 FEL Conference, Argonne, IL, 2002* [Nucl. Instrum. Methods Phys. Res., Sect. A **507**, 331 (2003)].
- [10] H. Loos *et al.*, *Proceedings of the 2003 FEL Conference, Tsukuba, Japan, 2003* [Nucl. Instrum. Methods Phys. Res., Sect. A **528**, 189 (2004)].
- [11] M. Huening and H. Schlarb, in Ref. [8], pp. 2074–2076.
- [12] D. H. Dowell *et al.*, in Ref. [3], pp. 1299–1301.
- [13] J. Rosenzweig *et al.*, Nucl. Instrum. Methods Phys. Res., Sect. A **341**, 379 (1994).
- [14] J. L. Adamski *et al.*, Proc. SPIE Int. Soc. Opt. Eng. **2988**, 158 (1997).
- [15] R. Akre *et al.*, in Ref. [3], pp. 2421–2423.
- [16] E. Jongewaard *et al.*, SLAC-PUB-7146, 1996.
- [17] Z. D. Farkas *et al.*, SLAC-PUB-1561, 1975.
- [18] J. Wu *et al.*, in Ref. [5], pp. 1156–1158.
- [19] R. Akre *et al.*, *Proceedings of the 2001 Particle Accelerator Conference, Chicago, IL* (IEEE, Piscataway, NJ, 2001), pp. 2353–2355.
- [20] C. Limborg-Deprey *et al.* (unpublished).
- [21] J. Qiang *et al.*, Phys. Rev. ST Accel. Beams **9**, 044204 (2006).
- [22] P. Emma *et al.*, in Ref. [3], pp. 807–809.